

WRF–SBM Simulations of Melting-Layer Structure in Mixed-Phase Precipitation Events Observed during LPVEx

TAKAMICHI IGUCHI,^{*,+} TOSHIHISA MATSUI,^{*,+} WEI-KUO TAO,⁺ ALEXANDER P. KHAIN,[#]
VAUGHAN T. J. PHILLIPS,[@] CHRIS KIDD,^{*,+} TRISTAN L'ECUYER,[&]
SCOTT A. BRAUN,⁺ AND ARTHUR HOU⁺

^{*} Earth System Science Interdisciplinary Center, University of Maryland, College Park, College Park, Maryland

⁺ Laboratory for Atmospheres, NASA Goddard Space Flight Center, Greenbelt, Maryland

[#] Department of Atmospheric Sciences, Institute of the Earth Science, The Hebrew University of Jerusalem, Jerusalem, Israel

[@] Department of Physical Geography and Ecosystem Science, Lund University, Lund, Sweden

[&] Department of Atmospheric and Oceanic Sciences, University of Wisconsin–Madison, Madison, Wisconsin

(Manuscript received 4 November 2013, in final form 8 September 2014)

ABSTRACT

Two mixed-phase precipitation events were observed on 21 September and 20 October 2010 over the southern part of Finland during the Light Precipitation Validation Experiment (LPVEx). These events have been simulated using the Weather Research and Forecasting Model coupled with spectral bin microphysics (WRF–SBM). The detailed ice-melting scheme with prognosis of the liquid water fraction during melting enables explicit simulation of microphysical properties in the melting layer. First, the simulations have been compared with C-band 3D radar measurements for the purpose of evaluating the overall profiles of cloud and precipitation. The simulation has some artificial convective patterns and errors in the forecast displacement of the precipitation system. The overall overestimation of reflectivity is consistent with a bias toward the range characterized by large-diameter droplets in the surface drop size distribution. Second, the structure of the melting bands has been evaluated against vertically pointing K-band radar measurements. A peak in reflectivity and a gradual change in Doppler velocity are observed and similarly simulated in the common temperature range from approximately 0° to 3°C. The effectiveness of the time-dependent melting scheme has been justified by intercomparison with a corresponding simulation using an instantaneous melting scheme. A weakness of the new melting scheme is that melting particles having high liquid water fractions on the order of 80%–90% cannot be simulated. This situation may cause underestimation of radar reflectivity in the melting layer because of the assumptions of melting-particle structure used to calculate the scattering properties.

1. Introduction

Ice particles melt not instantaneously but gradually when they fall through air layers having temperatures that are warmer than 0°C. The bright band (Austin and Bemis 1950), a thin horizontally oriented layer with relatively large radar reflectivity, is observed in a radar echo profile below the 0°C temperature level. This characteristic structure is often seen in radar signatures of mixed-phase stratiform clouds with rainfall at the surface. The high radar reflectivity in the melting layer is caused by a number of factors. A melting ice particle has

a dielectric constant that is different from those of pure ice or water particles with the same mass. If the ice particle is wrapped in water, the dielectric property of the particle becomes closer to that of a pure water particle. The backscattering cross section of the melting particle becomes larger than that of a pure water particle with the same mass in most radar wavelength ranges, since the maximum dimension of the melting ice particle remains large in comparison with that of the particle after complete melting. On the other hand, melting ice particles fall more slowly than water particles with the same masses. As a result, the particle number concentration in the melting layer tends to be larger than that beneath the melting layer. This effect additionally contributes to a relative increase in radar reflectivity within the melting layer. In addition to those two factors, the

Corresponding author address: Takamichi Iguchi, Mail Code 612, NASA Goddard Space Flight Center, Greenbelt, MD 20771.
E-mail: takamichi.iguchi@nasa.gov

following factors may have nonnegligible effects on forming the brightband reflectivity signatures (Fabry and Zawadzki 1995): change of hydrometeor particle size distribution (PSD) in the melting layer through deposition and aggregation growth near the top of the layer and raindrop breakup near the bottom (PSD change), irregular nonspherical shapes of melting hydrometeor particles (shape effects), and deflection of water distribution within or outside the melting particles (density effects; e.g., Zawadzki et al. 2005).

A better understanding of ice particle melting and subsequent brightband formation is key to reducing errors in rainfall-rate estimates from remotely sensed measurements through the retrieval algorithms (e.g., Smith 1986). The high backscatter signal in a bright band may be interpreted as the existence of high rainfall rates. Additional attenuation of the radar power in a bright band has a significant influence on the rainfall estimates when the radar signal passes through a strong bright band at a low elevation angle or in the case of millimeter-wavelength radar measurements (Matrosov 2008). Ice particle melting has a significant impact on the retrieval results from microwave emission measurements (e.g., Schols et al. 1995; Bauer et al. 1999, 2000). Cooling that is due to latent heat absorption by the melting process might have an impact on the mesoscale cloud dynamics (e.g., Tao et al. 1995; Heffernan and Marwitz 1996).

This unique structure of the bright band is an important subject to investigate not only in remotely sensed measurements but also in atmospheric models. It is difficult to explicitly simulate the microphysical structure of the melting layer in three-dimensional models. A one-dimensional model that specialized in representing a melting layer was often employed to analyze the structure, with the results then compared with actual measurements (e.g., Klaassen 1988; Szyrmer and Zawadzki 1999). A few studies, however, attempted similar approaches using a fully three-dimensional model. For example, Gallus and Pfeifer (2008) evaluated Weather Research and Forecasting (WRF) Model simulations at 2.8-km horizontal grid spacing using five different bulk microphysical schemes in comparison with the observed radar reflectivity. The simulations had large errors in reproducing the brightband part of the observed reflectivity signature.

There have been shortcomings in simulating a bright band in a fully three-dimensional model. Model simulations often do not have sufficient vertical resolution to resolve the distribution of melting particles. A complicated diagnostic model in bulk microphysics is additionally required to describe the melting process and the change of the particle structure to calculate the radar backscatter. Furthermore, the calculation of the radar

scattering by melting particles has a large uncertainty (e.g., Fabry and Szyrmer 1999).

This study is motivated by the following objectives in terms of brightband simulation: It is important to investigate how the brightband structure can be properly simulated using a fully three-dimensional high-resolution model with spectral bin microphysics containing a detailed melting scheme. The simulated results are compared with measurements for the cloud and precipitation distributions including the bright bands. Discussion about the limitations and faults in model performance is valuable for further improving the atmospheric model and the forward calculation of radar reflectivity. Also of significance is the investigation of the sensitivity of simulated brightband structure and the assumptions used to determine the scattering properties of melting particles. These theoretical assumptions are important components for the forward simulation of satellite precipitation measurements, for example, those associated with the Global Precipitation Measurement (GPM) mission (Matsui et al. 2013; Hou et al. 2014). For rainfall and latent heat retrievals from spaceborne observations, the detection of melting layers is a critical step in separating the types of clouds causing the precipitation, for example, stratiform or convective. In particular, the measurements made by the GPM *Core Observatory* satellite extend its observational range up to latitudes of 68°, beyond those covered by the Tropical Rainfall Measuring Mission; weak bright bands at low elevations are often observed in systems of mixed-phase light precipitation at mid- and high latitudes.

In this paper, we focus particularly upon mixed-phase stratiform precipitation events observed during the Light Precipitation Validation Experiment (LPVEx; L'Ecuyer et al. 2010). This field experiment was conducted in the vicinity of Helsinki, Finland, from 15 September to 31 December 2010. LPVEx was originally aimed at identifying the ability of spaceborne sensors to detect light precipitation and the accuracy of the associated retrieval algorithms. The scientific purpose also included improvement of the understanding of the light-precipitation mechanism with low-elevation melting layers at the high latitudes. A number of in situ and remotely sensed measurements were carried out, including ground-based disdrometers, radars, radiometers, ceilometers, sounding systems, and aircraft sampling using W-band radar and particle probes. One of the core strategies in LPVEx was to construct full three-dimensional depictions of rainfall scenes through the combination of multiple measurements.

This study utilizes the WRF Model coupled with spectral bin microphysics (WRF-SBM; Iguchi et al. 2012b) for the simulations of two particular precipitation events

during LPVEx; the SBM part is extracted from the Hebrew University Cloud Model (HUCM; [Khain et al. 2011, 2012](#)). A time-dependent melting scheme ([Phillips et al. 2007](#)) is installed in the HUCM SBM in place of an out-of-date instantaneous melting scheme. The SBM thus can simulate a more realistic melting process that includes an intermediate state between pure liquid and ice particles by predicting liquid water fraction (LWF) in melting particles. In contrast, in the outdated SBM ice particles are instantaneously converted into purely liquid particles with the same masses after passage down through the 0°C isotherm. This update is expected to significantly improve the simulation of the brightband structure without diagnostically assuming the scattering properties of melting particles.

This paper is organized as follows: The method containing the model description and experiment design is described in [section 2](#). The simulation results and a comparison with measurements are discussed in [section 3](#). The summary and conclusions are given in [section 4](#). The [appendix](#) provides a discussion on the sensitivity of radar backscattering efficiency to melting-structure model, particle size, and LWF.

2. Method

a. Description of WRF-SBM

The WRF Model is a regional weather forecasting system that was developed primarily by the National Center for Atmospheric Research ([Dudhia 1989](#)). In this study, the Advanced Research configuration of WRF, version 3.4, has been coupled with the HUCM SBM (e.g., [Khain et al. 2011, 2012](#)). In the SBM, hydrometeor particle types are categorized into seven classes: water droplets, ice crystals (plate, column, and dendrite), snow aggregates, graupel, and hail. The PSD of each class is discretely represented in 43 doubling mass bins covering particle mass limits in a range from 3.35×10^{-11} to 1.47×10^2 g (or $2 \mu\text{m} < \text{radius} < 32.8$ mm as equivalent droplet radii). The PSD of condensation nuclei (CN) is discretized into a mass grid that contains 13 bins; the use of a smaller number of CN bins than that of the original HUCM SBM (43 bins) is to improve the efficiency of computation. Nucleation of droplets from CN is explicitly calculated on the basis of the Köhler curve theory ([Köhler 1936](#)). Changes in the hydrometeor PSDs are calculated for every time step by considering the following cloud microphysical processes as well as advection and fall under gravity: nucleation of droplets and ice crystals, condensation and deposition growth, evaporation, sublimation, freezing, riming, melting, shedding, coalescence growth, and breakup.

b. Melting model in the SBM

The ice-melting scheme in HUCM SBM was largely updated in [Phillips et al. \(2007\)](#); the outdated instantaneous melting model was replaced with the new time-dependent melting model. Supplementary mass size distributions representing LWF on melting ice crystals, snow aggregates, graupel, and hail have been added into the sets of 43 bins; LWF is defined as the mass ratio of water on/in the melting ice particle to the original unmelted ice particle ([Mitra et al. 1990](#)). The theoretical model and equations for the melting of snow are based on those in [Mitra et al. \(1990\)](#) and are used to describe the thermodynamics and the conservation of mass among the three phases of water. The corresponding model and equations in [Rasmussen and Heymsfield \(1987\)](#) are used to calculate the melting processes of graupel and hail with water shedding. If melting particles return to a layer that has a temperature below 0°C, the liquid parts of melting particles freeze again immediately and simultaneously the value of LWF resets to zero. In this study, the time-dependent melting model for ice crystals is eliminated to improve computational efficiency since such small particles do not contribute to the bulk of the radar signature. Ice crystals are set to melt immediately and completely in the layer with a temperature above 0°C.

In the subsaturated environment for ice, the onset of melting is delayed by sublimation even if the ambient temperature is over 0°C. The skin temperature of the ice particle is affected by latent heat exchanges that are due to sublimation/deposition and by the ambient temperature before melting starts. The ice skin temperature T_s under the ambient temperature T_e is iteratively computed by the following equation before T_s reaches 0°C [[Mitra et al. 1990](#); [Pruppacher and Klett 1997](#), their Eq. (13-92); [Phillips et al. 2007](#)]:

$$T_s = T_e - \frac{L_s D_v M_w}{k_a R} \left[\frac{e_{\text{sat},i}(T_s)}{T_s} - \frac{\phi_v e_{\text{sat},w}(T_e)}{T_e} \right], \quad (1)$$

where L_s is the latent heat of sublimation, k_a is the heat conductivity of air, D_v is the diffusivity of water vapor in air, M_w is the molecular weight of water, R is the universal gas constant, ϕ_v is the fractional relative humidity of air, and $e_{\text{sat},w}$ and $e_{\text{sat},i}$ are the saturation vapor pressure over water and ice planes, respectively; the ventilation coefficients of vapor and heat transfers are assumed to be identical.

After melting starts, the skin temperature of the melting particle is determined by latent heat exchanges due to the sublimation and melting of the ice part and the evaporation of the liquid part below the ambient

temperature. In the melting model of [Mitra et al. \(1990\)](#), latent heating by sublimation of the ice part is not considered when the melting has already started. The reduction rate in the mass of the ice part of the melting snow is given by the following equation [[Mitra et al. 1990](#); [Pruppacher and Klett 1997](#), their Eq. (16-83); [Phillips et al. 2007](#)]:

$$-\frac{dm_i}{dt} = \frac{4\pi C_i f_L}{L_m} \left\{ k_a (T_e - T_0) + \left(\frac{D_v L_e M_w}{R} \right) \left[\frac{\phi_v e_{\text{sat},w}(T_e)}{T_e} - \frac{e_{\text{sat},w}(T_0)}{T_0} \right] \right\}, \quad (2)$$

where C_i is the capacitance of the melting snowflake, f_L is the mean ventilation coefficient for vapor and heat diffusions, and L_m and L_e are the latent heats of melting and evaporation, respectively; T_0 is 0°C . The ragged surface of the snow is uncovered by meltwater in their model assuming no shedding and breakup.

For graupel and hail, the melting process is divided into a soaking stage and a fully soaked stage, according to whether meltwater stays only inside the ice or flows to the exterior ([Phillips et al. 2007](#)). The basic equations describing the changes of skin temperatures and the ice reduction rates of graupel and hail are similar to Eqs. (1) and (2) on the basis of the calculation of the heat transfer, except for different ventilation coefficients for vapor and heat diffusions. At the soaking stage, meltwater exists inside the ice fringe of graupel or hail; the particle shape is assumed to be spherical. The terminal fall velocity is calculated using the hypothetical Reynolds number obtained on the assumption that the same particle is fully frozen. At the fully soaked stage, meltwater is assumed to be distributed in the form of a spherical shape around the particle for the formulation of the heat-transfer calculation. Shedding of meltwater occurs when the outflow mass exceeds a critical equilibrium value; the behavior is dependent on the particle Reynolds number ([Rasmussen et al. 1984](#)). The terminal fall velocity is determined by the interpolation between the values at the just-fully soaked stage and at the shedding stage ([Rasmussen and Heymsfield 1987](#)).

c. Radar simulator in the Goddard Satellite Data Simulator Unit

For a straightforward comparison between the model simulations and radar measurements, the corresponding radar products are calculated using an offline radar simulator module of the Goddard Satellite Data Simulator Unit (G-SDSU; [Matsui et al. 2009, 2013](#)). The method used to calculate the radar reflectivity factor is based

mostly on that of [Masunaga and Kummerow \(2005\)](#). The PSD and LWF of the hydrometeors simulated in the WRF-SBM are input directly into the radar simulator. The particle backscattering cross section is calculated on the basis of a full-solution Mie-based routine. Note that the radar simulator provides the attenuated radar reflectivity from the simulated hydrometeors so that the observed radar echo profile without attenuation correction is used as an equivalent for the comparison.

The complex dielectric constant and the bulk diameter of the particle are principal parameters to determine the single-scattering properties in the Mie-based routine in G-SDSU. The simulator has several options for the assumption of melting-particle structure to calculate the dielectric properties. Two types of functions, Maxwell Garnett (MG) dielectric function of 2-component media ([Maxwell Garnett 1904](#); [Bohren and Battan 1982](#); [Olson et al. 2001](#)) and effective-medium (EM) dielectric function ([Bohren and Battan 1980](#)) based on the assumption of homogenous mixing, are available in the present simulator. Furthermore, two types of model representing the state of water and ice inclusion are available in the calculation using the MG function: 1) ice and water are assumed to be the inclusion and the matrix, respectively (MG1), and 2) the reverse of the first model (MG2). The complex dielectric constant of a melting particle is calculated using the following equation ([Olson et al. 2001](#)):

$$\epsilon_{\text{mix}} = \frac{(1 - f_{\text{inc}})\epsilon_{\text{mat}} + f_{\text{inc}}\zeta\epsilon_{\text{inc}}}{1 - f_{\text{inc}} + f_{\text{inc}}\zeta}, \quad \text{where} \\ \zeta = \left(\frac{2\epsilon_{\text{mat}}}{\epsilon_{\text{inc}} - \epsilon_{\text{mat}}} \right) \left[\left(\frac{\epsilon_{\text{inc}}}{\epsilon_{\text{inc}} - \epsilon_{\text{mat}}} \right) \ln \left(\frac{\epsilon_{\text{inc}}}{\epsilon_{\text{mat}}} \right) - 1 \right], \quad (3)$$

ϵ is the complex dielectric constant, and f is the volume fraction of the component; the subscripts mix, mat, and inc denote the parameters of the mixture, matrix, and inclusion materials, respectively. The LWF that was forecast in the WRF-SBM determines the volume fractions of ice and water in the melting particle.

The following model is set as the standard option: the second model for the MG function (MG2) is applied to the calculation of the single-scattering properties of melting snow aggregates in the SBM since the assumption of the melting-particle structure is most consistent with that in the SBM ([Mitra et al. 1990](#)). On the other hand, MG1 is used for the calculation of the single-scattering properties of melting graupel and hail in the SBM for the same reason. The results calculated using this setting are mainly discussed in this paper, but we briefly show the sensitivity of the backscattering efficiency of a snow aggregate on the particle size, the LWF, and the assumption of the melting-particle structure in the [appendix](#).

The bulk ice volume, except for the meltwater part in a melting particle, is considered as a mixture of ice and air. The complex dielectric constant of the ice volume is calculated using the MG model [Eq. (3)] regarding it as a mixture of ice and air; ice and air are assumed to be the inclusion and the matrix in the present simulator, respectively. This calculation method is applied to cases of both melting and unmelting ice particles. The volume fractions of the ice and air in Eq. (3) are determined on the basis of the bulk density of the original ice particle. Because the density change of snow aggregates by riming is considered in the SBM (Khain et al. 2012; Iguchi et al. 2012b), the prognostic rimed fraction in each mass bin of snow is used to determine the volume fractions of ice and air. The diagnostic bulk density of snow is used to decide the bulk diameter for the calculation in the Mie-based routine. The bulk diameter decreases with increases in the fractions of rimed and liquid components in the melting particle.

The G-SDSU can simulate the mean Doppler velocity that is equivalent to the first moment of a Doppler reflectivity spectrum (e.g., Atlas et al. 1973). If the radar is vertically pointing, the mean Doppler velocity is expressed in the form of the mean reflectivity-weighted vertical velocity of the particles. A numerical expression of the velocity is given by the following equation (downward is positive):

$$v_d = \frac{\int_{r_{\min}}^{r_{\max}} dn(r)/dr \times C_{\text{bk}}(r)[v_f(r) - U] dr}{\int_{r_{\min}}^{r_{\max}} dn(r)/dr \times C_{\text{bk}}(r) dr}, \quad (4)$$

where U is the upward vertical wind velocity, r is the radius of the particle, n is the number concentration of particles with a radius of less than r , C_{bk} is the back-scattering cross section, and v_f is the falling velocity of the particle. Here, $v_f(r)$ is set to be equivalent to the function of the relation between the terminal fall velocities and the hydrometeor sizes used in the SBM.

d. Design of numerical experiments

Two light-rainfall events were observed on 21 September and 20 October 2010 over Helsinki. To reproduce these events, 36-h simulations were conducted from 1200 UTC 20 September to 0000 UTC 22 September and from 1200 UTC 19 October to 0000 UTC 21 October. Three simulation domains were constructed with horizontal grid intervals of 9, 3, and 1.5 km; the second domain (domain 2) and the third domain (domain 3) were nested within the first domain (domain 1). Time steps of 54, 18, and 6 s were set for the simulations on the three

domains, respectively. The vertical domain up to a height of approximately 20 km was divided into 60 layers with intervals increasing with altitude; for example, the layer thicknesses at 1- and 2-km height above sea level, which were close to the heights of freezing levels on the targeted days, were approximately 88 and 194 m, respectively. The following options for physical processes were employed in the experiments: Mellor–Yamada–Janjić level-2.5 turbulent closure model (e.g., Janjić 1990) for the planetary boundary layer process in domain 1 and domain 2 and Mellor–Yamada–Nakanishi–Niino model (Nakanishi and Niino 2004) in domain 3, the “Noah” land surface model with four-layer soil structure to calculate heat and moisture fluxes over the land surface, and the Goddard radiation package for both shortwave and longwave radiations for all domains.

The simulation for each domain was individually conducted. An offline one-way nesting was applied to connect the simulations from the parent domain to the nested domain. The initial conditions of all domains and the time-varying lateral boundary condition of domain 1 were calculated from the interim reanalysis data of the European Centre for Medium-Range Weather Forecasts model (Dee et al. 2011) with a spectral T255 horizontal resolution. The simulations for domain 2 and domain 3 were conducted using the outputs of the first and second domain simulations, respectively. The time-varying lateral boundary condition of the basic prognostic variables except for hydrometeors was prepared in the one-way nesting configuration.

In the domain-1 simulation, one-moment bulk cloud microphysics of the Goddard Cumulus Ensemble model (e.g., Lang et al. 2007) was employed together with the Grell–Devenyi ensemble cumulus parameterization (Grell and Devenyi 2002). In the domain-2 and domain-3 simulations, the HUCM SBM was employed without cumulus parameterization. The simulation result of domain 3 was archived in the form of three-dimensional volume per hour for all model grids of the domain, containing all hydrometeor PSD, riming fractions of snow aggregates, and LWFs of melting particles as well as the standard prognostic and diagnostic variables.

In domains 2 and 3, the initial CN size distribution was set on the basis of an empirical relationship between the number concentration of activated CN and supersaturation [Eq. (1) in Iguchi et al. 2012b]. The values $N_0 = 1500 \text{ cm}^{-3}$ and $k = 0.5$ in the equation were used for this numerical experiment; these values were determined as typical values for the continental environment with less pollution (Khain et al. 2010). The initial concentration was uniformly distributed in the vertical layers under 2 km and decreased exponentially with a scale height of 2 km above.

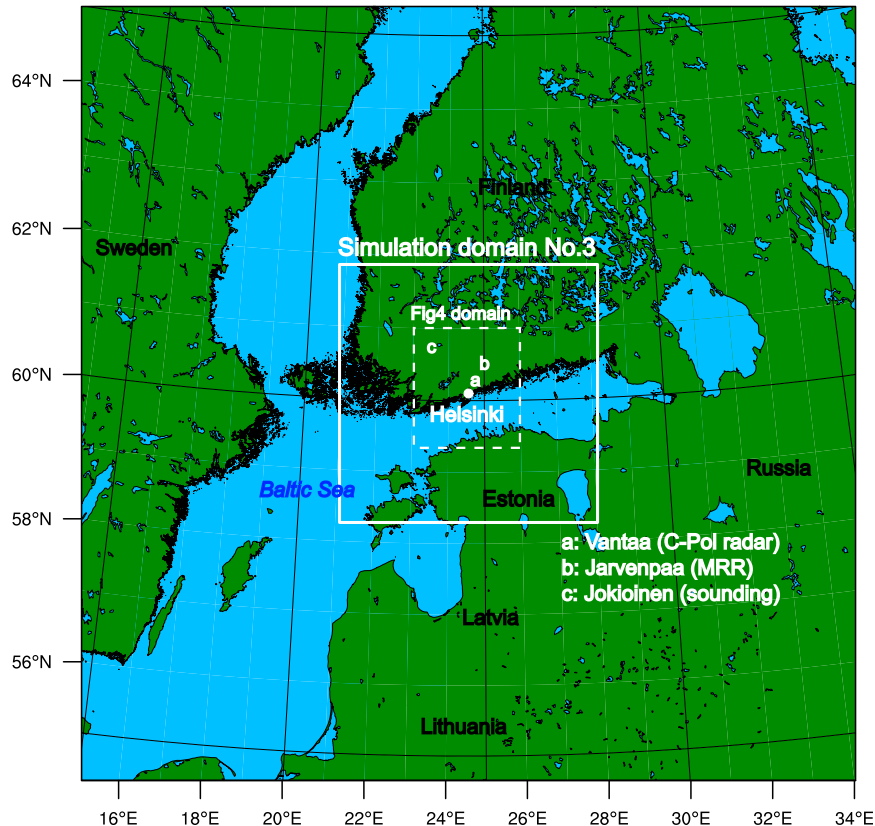


FIG. 1. Domain configuration of the WRF-SBM simulations. The whole area of the map corresponds to simulation domain 2 with horizontal grid intervals of 3 km. The area enclosed by the white-solid-line square shows the third domain with horizontal grid intervals of 1.5 km. The area denoted by the white dotted line shows the whole domain of Fig. 4. The white dot at the center denotes the location of Helsinki. The letters from a to c on the third domain denote the locations of the observation sites, Vantaa (60.16°N , 24.52°E), Jarvenpaa (60.3°N , 25.05°E), and Jokioinen (60.8°N , 23.5°E), respectively.

Another set of WRF-SBM simulations was conducted using the same experimental design but turning off the time-dependent melting scheme of snow aggregates, graupel, and hail. In these experiments, solid particles were instantaneously melted and converted into liquid particles with the same masses when entering layers that were warmer than 0°C (instantaneous melting scheme). These additional simulation results were used to comparatively highlight and investigate effects of the new time-dependent melting scheme.

3. Results

a. An overview of the selected precipitation events

On 21 September 2010, a low pressure system with associated widespread rain approached from the southwest, covered the southern part of Finland, and then passed to the northeast. Continuous rainfall occurred at

the Jarvenpaa site (60.3°N , 25.05°E) (Fig. 1) from about 0400 to 1930 UTC and was measured by the two-dimensional video disdrometer (2DVD) and the laser optical Particle Size and Velocity (Parsivel) disdrometer (Löffler-Mang and Joss 2000) deployed at the site. The surface rainfall rate was mostly less than 4 mm h^{-1} (Fig. 2a); the average rate of the sampled rainfall was 0.89 mm h^{-1} . On 20 October, a synoptic-scale cyclonic system was developing over the Norwegian Sea (approximately 65°N , 0°) and stratiform cloud with light rainfall on its eastern fringe passed over the southern part of Finland from south to north; continuous weak rainfall was observed from 0700 UTC at the Jarvenpaa site (Fig. 2b). The surface rainfall rate was generally less than 2 mm h^{-1} ; the average sampled rainfall rate was 0.42 mm h^{-1} .

Figure 2 shows time series of the surface rainfall rate at the coordinates of the Jarvenpaa site in the WRF-SBM simulation as well as the measured values of the 2DVD and Parsivel disdrometer. In the 21 September

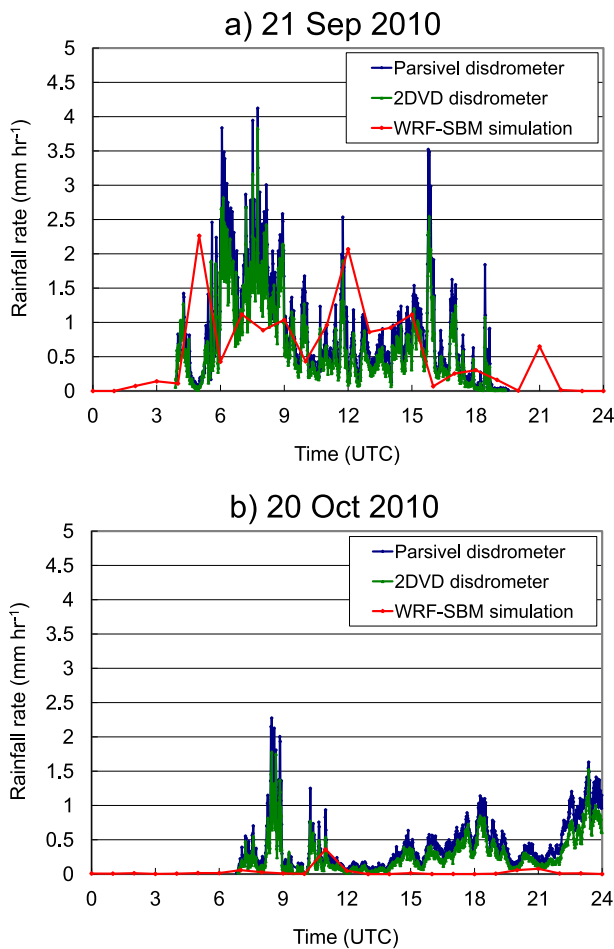


FIG. 2. Time series of the surface rainfall rates at the Jarvenpaa site (60.3°N, 25.05°E) measured by the Parsivel disdrometer and 2DVD and the WRF-SBM simulations on (a) 21 Sep and (b) 20 Oct 2010.

case, the simulated values are approximately 2.3 mm h^{-1} or less. The onset of rainfall is reproduced reasonably well, whereas the end is delayed for approximately 3 h. The simulation generally underestimates the rainfall rate at the coordinates, whereas relatively strong rainfall is simulated at the western side of the simulation domain around 1200 UTC with maximum hourly rainfall rates of approximately 8 mm h^{-1} . In the 20 October case, very weak rainfall of less than 0.3 mm h^{-1} is intermittently simulated at the coordinates. The horizontal distribution of the simulated rainfall shows that the central part of the simulation domain including the Jarvenpaa site has little rainfall. Stronger rainfall is simulated on the eastern and western sides of the domain, however; the maximum hourly rainfall rate is less than $\sim 5 \text{ mm h}^{-1}$.

Figure 3 shows vertical profiles of air temperature every 12 h on both days derived from the sounding vdata at the Jokioinen site (60.8°N, 23.5°E) and from the

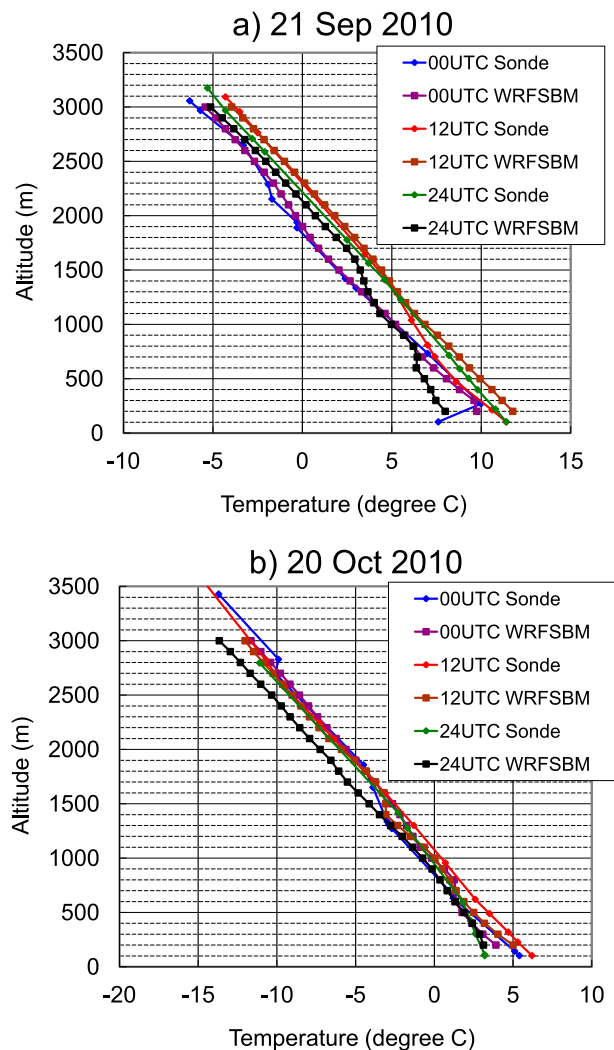


FIG. 3. Vertical temperature profiles from the sounding data and the WRF-SBM simulation at the Jokioinen site (60.8°N, 23.5°E) on (a) 21 Sep and (b) 20 Oct 2010. (Sounding data were provided by the Dept. of Atmospheric Science of the College of Engineering at the University of Wyoming.)

WRF-SBM simulations. On 21 September (Fig. 3a), the height of the freezing level (0°C level) was observed at approximately 1850 m at 0000 UTC and increased to 2300 m at 1200 and 0000 UTC on the next day. This variation is probably due to the airmass transition associated with the passing of the precipitation system. The simulation reproduces the temporal change of the freezing level; the difference of the freezing levels between the sounding data and the simulation is approximately 100 m at most. On 20 October, the height of the freezing level was around 1000 m all day (Fig. 3b). The simulation reproduces the height of the freezing level with a difference of 100 m, and the temperature around the freezing level is simulated with a difference of $\pm 1^\circ\text{C}$.

b. Macroprofiles of cloud and precipitation against C-Pol 3D radar measurements

Three dual-polarized C-band (C-Pol) Doppler radars were operated in a 3D mode (3D radar coverage by the elevation, range, and azimuth information) within the Helsinki Mesoscale Testbed (Dabberdt et al. 2005) during the LPVEx campaign. One of them, the Vantaa (VAN) 5.65-GHz radar, was deployed together with other types of radars and instruments at 60.16°N, 24.52°E. This radar performed simple volume scans by completing volume coverage patterns during the LPVEx campaign. The scanned reflectivity signature of the radar was arranged as sequential data on three-dimensional Cartesian coordinate grids with a 200-km horizontal domain and a 10-km vertical top height with 15-min intervals; the reflectivity data were interpolated on grids with horizontal intervals of 1 km and vertical intervals of 500 m.

The VAN radar data were used to validate the macroprofiles of cloud and precipitation distribution in the WRF-SBM simulations. Figures 4a and 4c show the horizontal distribution of the observed vertically maximum reflectivity Z_{\max} at 0600, 1200, and 1800 UTC 21 September and 20 October. On 21 September (Fig. 4a), the plot domain was generally covered with widespread homogeneous reflectivity of approximately 15 dBZ at 0600 and 1200 UTC. Relatively large reflectivities of more than 25 dBZ were centered and distributed toward the western side at 0600 UTC and then scattered at 1200 UTC. These were identified as relatively developed regions within the whole widespread rainfall system. At 1800 UTC, the precipitation system had mostly passed to the northeast with the southwestern segment of the domain having cleared. On 20 October (Fig. 4c), scattered precipitation started to appear over the region at 0600 UTC. The eastern side of the domain was continuously covered with precipitation that was slowly spreading from the west at 1200 and 1800 UTC. The magnitude of the maximum reflectivity was generally constant, ranging from approximately 5 to 25 dBZ. The clouds were advected from south to north by the synoptic airflow.

Figures 4b and 4d illustrate the corresponding snapshots showing Z_{\max} distribution calculated from the outputs of the WRF-SBM simulations through the radar simulator. In the 21 September case, the simulation reasonably reproduces the observed radar reflectivity coverage of cloud and precipitation on that day. This agreement in the reflectivity coverage is consistent with the similar duration of surface rainfall as measured by the disdrometers and the simulation at the Jarvenpaa site (Fig. 2a). The simulation overestimates Z_{\max} overall,

however, and has some locational errors in the forecasting of the precipitation system. The simulated precipitation system seems to be more convective rather than stratified with homogeneous Z_{\max} distribution as compared with the observed system. In the 0600 UTC plot, the simulated result shows overestimation of Z_{\max} , especially over the western side of the plot domain, where Z_{\max} is partly up to 40 dBZ. In the 1200 UTC plot, there are two clusters of large Z_{\max} distributions that are not seen in the observations. One is located on the eastern side of the domain with Z_{\max} up to 35 dBZ, and another is on the western side with Z_{\max} over 40 dBZ. In the 1800 UTC plot, the simulation generally reproduces the movement of the system, whereas the magnitude of Z_{\max} is partly overestimated in the northeastern segment, similar to the plots at 0600 and 1800 UTC. Some additional spotty patterns are simulated in the southwestern segment in error; these patterns are caused by convective clouds at lower levels than those of the relatively homogenous system in the northeastern segment.

In the 20 October case, the simulation plots highlight some forecast displacement errors in the region and coverage of the cloud and precipitation. Spotty patterns of low-level convective clouds are partly simulated, indicating more unstable atmospheric conditions, similar to the plot at 1800 UTC 21 September. In the 0600 UTC plot, the distribution of the simulated reflectivity covers even the northern part of the domain. Spotty echoes are artificially simulated over the western side. In the 1200 UTC plot, the extents of the observed and simulated reflectivities are relatively similar, except that spotty patterns remain over the northwest and the simulated Z_{\max} distribution has very small values of less than 5 dBZ over the area approximately from 24° to 25°E. At 1800 UTC, the location of the simulated echo is biased toward the eastern side from 25°E. This location bias results in significant underestimation of the simulated surface rainfall at the Jarvenpaa site around 1800 UTC and later (Fig. 2b). Some sparse echoes are simulated over the western segment.

Figure 5 illustrates the contoured frequency diagrams of the probability density distribution for altitude versus C-band radar reflectivity. These diagrams show the three-dimensional distributions of the observed and simulated reflectivities averaged for the entire domain and day. The heights of freezing levels are roughly 2 km on 21 September and 1 km on 20 October (Fig. 3). Overall, the diagrams of the observation results (Figs. 5a,d) show that the reflectivity gradually decreases with height above the freezing level, whereas a relatively constant profile of the probability density distribution is seen below the freezing level in both cases. The maximum value of the reflectivity is approximately 30 dBZ, which is seen

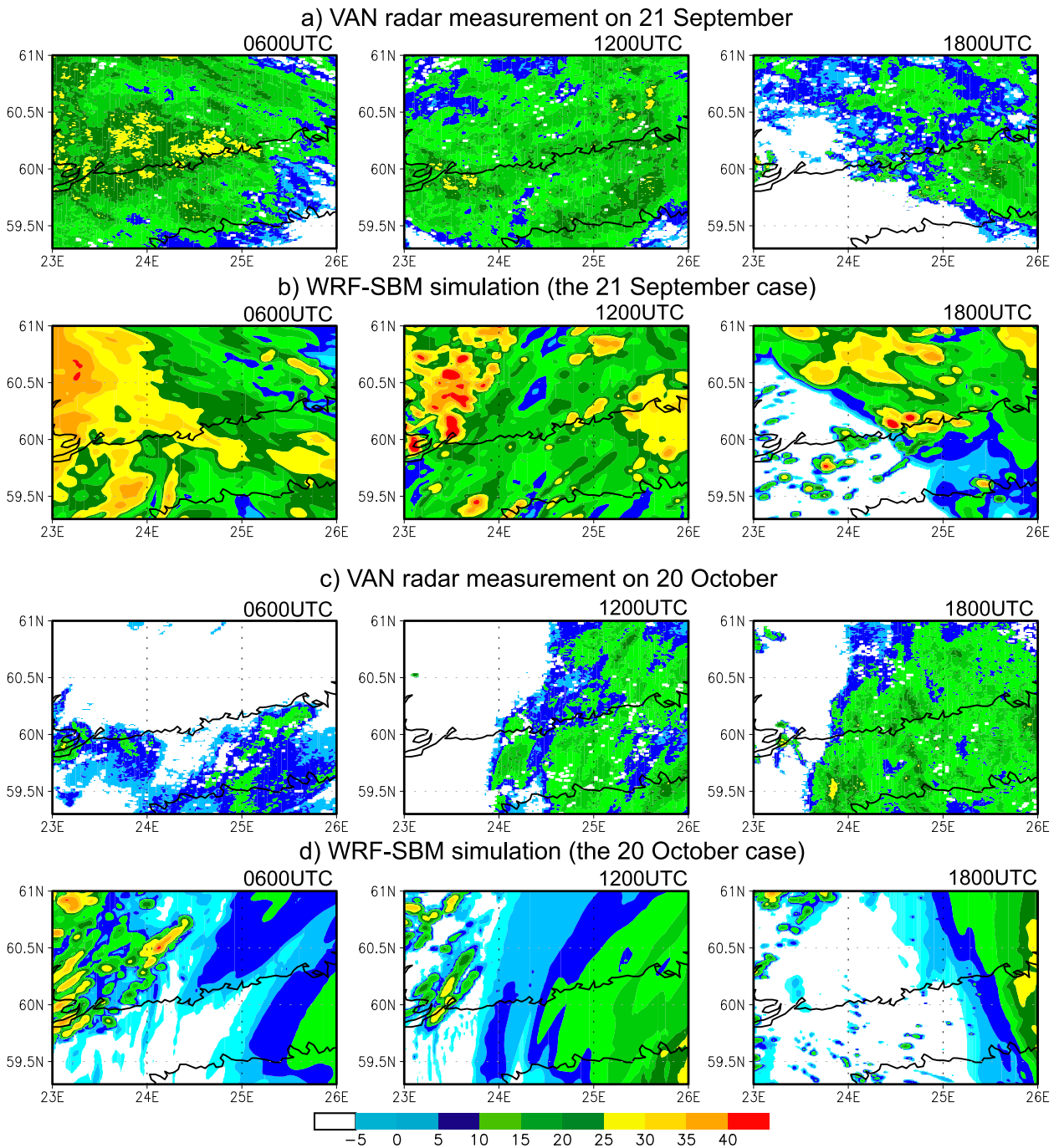


FIG. 4. Snapshots of horizontal distribution of maximum vertical C-band radar reflectivity (dBZ) (a),(c) derived from the Vantaa C-Pol 3D radar measurements and (b),(d) taken from the WRF-SBM simulations.

under the freezing level. There are no particular peaks resulting from the brightband effect under the freezing levels in the diagrams. The C-band radar, usually purposed to provide a horizontal view of the cloud and precipitation system, was operated in a 3D mode with a variety of elevation angles and beam spreading. As

a result, the brightband effect was likely to be smoothed out when mapped onto the three-dimensional Cartesian coordinate grids with coarse vertical resolution and further smoothed through combining all of the data into the individual diagrams. This feature can be confirmed by checking the same diagrams but sampling only over the

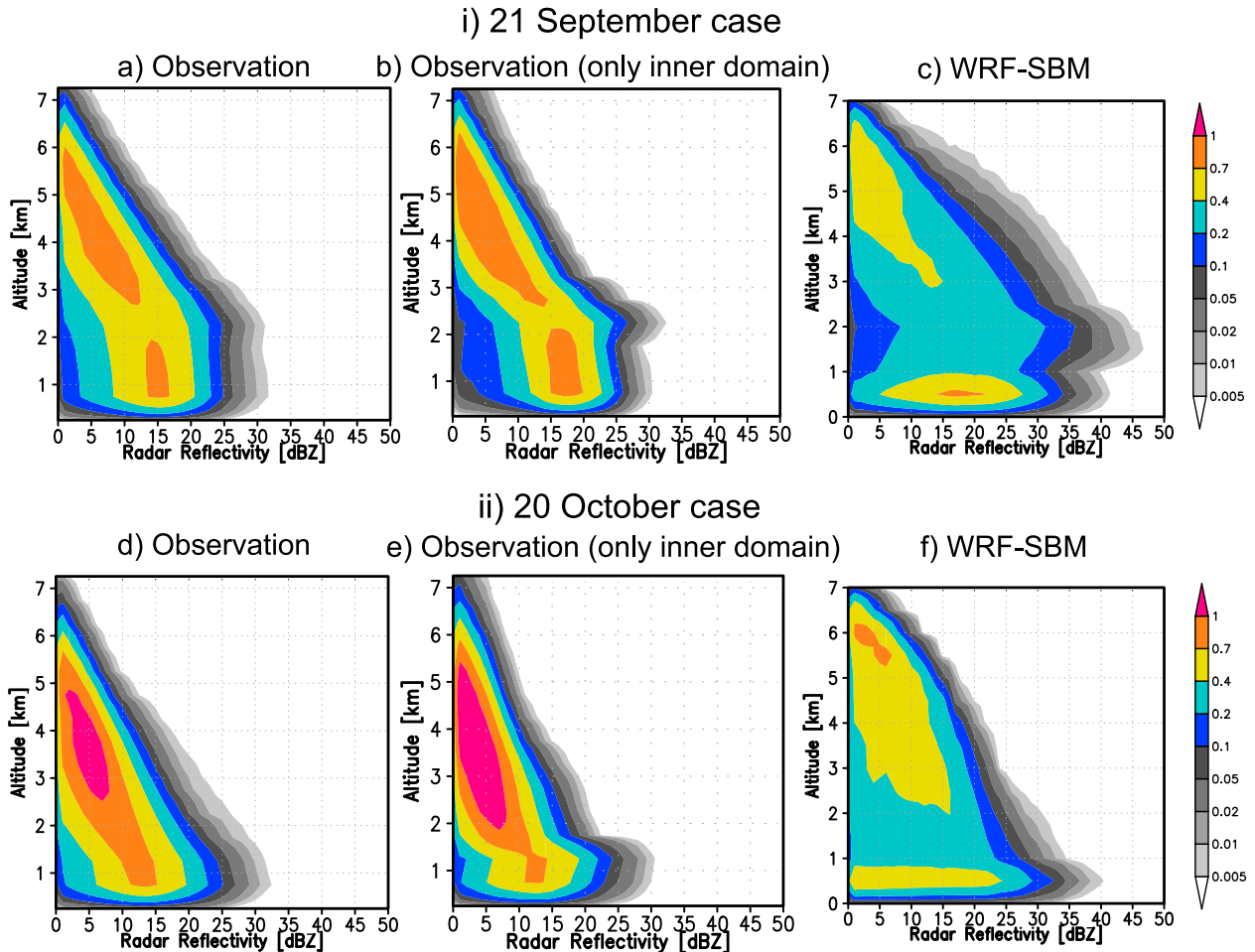


FIG. 5. Contoured frequency (%) diagrams normalized with both altitude and reflectivity in the 21 Sep case, derived from (a) the Vantaa C-Pol 3D radar measurements (sampling the square domain, 200 km on a side), (b) the same measurements but only sampling the square domain 50 km on a side around the radar location, and (c) the WRF-SBM simulations; (d)–(f) as in (a)–(c), but for the 20 Oct case.

area near the radar deployment (Figs. 5b,e). When compared with the diagrams that use all of the data, slight peaks in the observed reflectivity profiles are seen roughly at the heights of the freezing levels on those days. These increases in reflectivity are considered to be due to the brightband effect; the effect is evident as the sampling targets data only with high elevation angles. Bright bands are resolved more clearly with scanning at a higher elevation angle, because the vertical structure of the radar scattering can be captured more precisely with the relatively narrower beams. Although a sign of the brightband effect can be seen in the limited data sampling, the observations are not suited for detailed analysis of the bright bands because of the coarse vertical resolution with a variety of elevation angles and beam spreading. A detailed comparison and discussion about the brightband structure is given in section 3c, which describes the measurements by a vertically pointing radar.

Figures 5c and 5f show the corresponding probability density distribution obtained from the simulation results. The distributions are generally biased toward large reflectivities at most levels in comparison with those of the observations. The high-probability part is biased toward low altitudes of less than 1 km and high altitudes over 3 km. The high probability of low-altitude echo is identified in the form of artificial spotty patterns in the snapshots of Z_{\max} (Figs. 4b,d).

In the 21 September case (Fig. 5c), the probability of the simulated peak reflectivity is shifted toward larger reflectivities at a height of 2 km. A similar increase is identified at a height of 500 m in the 20 October case (Fig. 5d). These increases in reflectivity are due to brightband effects under the freezing levels. Overall, these heights have the peak reflectivities over the entire range of vertical levels Z_{\max} as shown in Figs. 4b and 4d, mostly originating from the reflectivities at these

heights; that is, the overestimation of Z_{\max} is partly due to the brightband effect that is barely resolved in the observation. The overestimation of reflectivity is distributed across almost all levels, however, and not only at the brightband heights. The cause of the overestimation is discussed in the comparison with the ground-based disdrometer measurements in section 3c. A similar problem of reflectivity overestimation was reported in other case-study simulations using a similar SBM for midlatitude mixed-phase clouds (Iguchi et al. 2012a).

The radar simulator that was used here can only provide radar products for vertically pointing systems. It does not strictly reproduce the 3D field of reflectivity provided by an actual radar scanning system with a variety of elevation angles, pulse lengths, and beam spreading. The simulated 3D field of the ground-based radar's echo is alternatively composed of zenith-pointing signals spread over the horizontal grids of the domain. This shortcoming of the present radar simulator causes some differences between the observed and simulated radar signatures. One of the notable differences is the representation of the brightband structure (Fig. 5). Increases in reflectivity that are due to the brightband effect are generally smoothed out in the observation diagrams for all data, whereas corresponding increases in reflectivity clearly appear in the simulation diagrams. The overestimation of reflectivity at the heights of the melting levels is regarded as an artificial error that results from the shortage of functions in the present radar simulator. This shortcoming prevents detailed discussion about microphysical insight that may be derived through analyses of polarimetric moments, differential reflectivity ZDR, and other parameters. Note that this deficiency in the present simulator is not important for the purposes of evaluating the macroprofiles of the simulated cloud and precipitation in this section, however, even though it has a nonnegligible impact on detailed analysis of the vertical structure around the bright band.

c. Vertical profiles against Micro Rain Radar

1) ANALYSIS OF RADAR REFLECTIVITY AND DOPPLER VELOCITY PROFILES

Vertically pointing Micro Rain Radars (MRR; e.g., Peters et al. 2002) were deployed at three ground sites (Emasalo, Harmaja, and Jarvenpaa) as well as on Research Vessel (R/V) *Aranda* during the LPVEx campaign. The MRR is a frequency-modulated continuous-wave (FM-CW) Doppler radar. The transmit frequency is 24.15 GHz so that Rayleigh scattering is not applicable to large rain-droplet sizes. A 1-min sampling interval and 100-m vertical resolution up to 3-km altitude were set for the LPVEx field experiment.

The equivalent radar reflectivity factor is calculated by the following equation using the measured spectral reflectivity (METEK 2009):

$$Z_e = \frac{\lambda^4}{\pi^5 |K^2|} \int \eta(f) df, \quad (5)$$

where λ is the radar wavelength and $\eta(f)$ is the spectral reflectivity at frequency f . We set $|K^2|$ at 0.92 for all vertical layers, and hence Z_e is identical to the water equivalent radar reflectivity factor Z_{ew} . Because the types of the scattering particle cannot be distinguished in the measurements, Z_{ew} is used as a standard parameter for the reflectivity factor. Comparison between equivalent radar reflectivity factors is valid only if they are calculated using the same value of $|K^2|$.

The first moment of the Doppler reflectivity spectrum (the mean Doppler velocity for short) is expressed by the following equation (METEK 2009):

$$v_d = \frac{\lambda}{2} \frac{\int \eta(f) f df}{\int \eta(f) df}. \quad (6)$$

Since the equation can be converted from the form with the differential of frequency (df) into that with the differential of particle size (e.g., dr), Eq. (6) is basically equivalent to Eq. (4).

Figure 6 illustrates time–height indicators of Z_{ew} and v_d measured by the MRR at the Jarvenpaa site. The time series of the reflectivity profiles (Figs. 6a,c) show slight increases in the reflectivity below the freezing level on both days, which are identified as bright bands. The heights are at approximately 1900 m on 21 September and 700 m on 20 October; these vertical structures of the reflectivity and velocity are almost homogeneous for certain periods; the durations are in agreement with those of the surface rainfall measured by the collocated disdrometers (Fig. 2). The patchy pattern of very small reflectivities above the height of 1 km is considered to be background instrumental noise. On 21 September, the reflectivity below the bright band is slightly smaller than those at the lower altitudes because of the attenuation of radar signals by hydrometeors in the cores of the precipitation systems.

The dependence of the variables on height is summarized in the panels of normalized contoured-frequency-by-altitude diagrams (CFAD; Yuter and Houze 1995) (Fig. 6). The increases in reflectivity under the freezing levels indicate the brightband effect. The bright band extends to approximately 1500–2100 m on 21 September and 400–1000 m on 20 October. The tops of the bright band

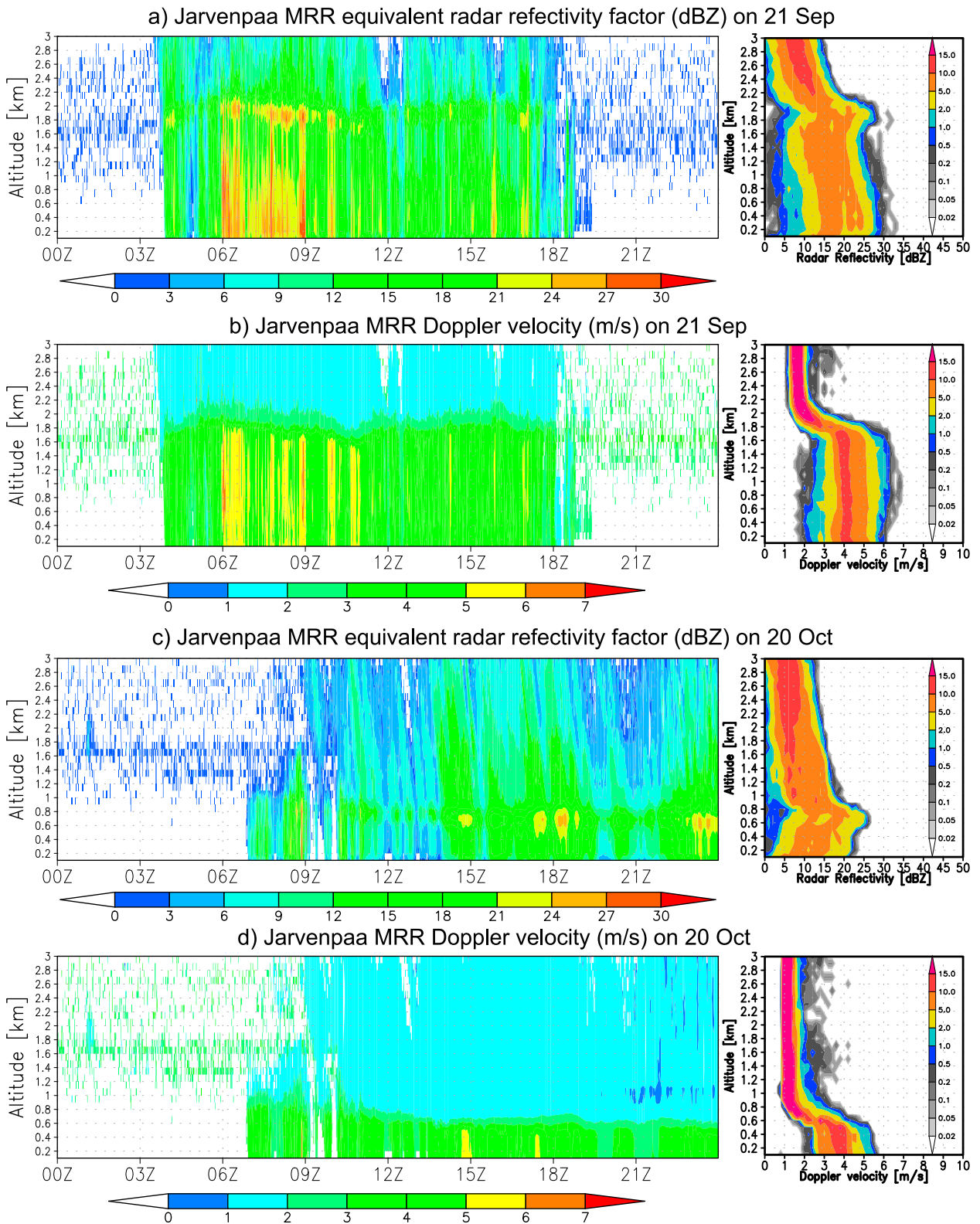


FIG. 6. Time–height cross sections of the (a),(c) water equivalent radar reflectivity factor (dBZ) and the (b),(d) mean Doppler velocity (ms^{-1}) derived from the measured spectral reflectivity of the MRR at the Jarvenpaa site. (right) The corresponding CFADs of the parameters, sampled over the time range (top) from 0400 to 1800 UTC 21 Sep and (bottom) from 0900 20 Oct to 0000 UTC 21 Oct to exclude clear sky with background instrumental noises.

correspond roughly to the heights of the freezing levels estimated from the temperature profiles at the Jarvenpaa site (Fig. 3).

The mean Doppler velocity has small values from 1 to 2 m s^{-1} above the melting layer, whereas the velocity is roughly from 2 to 7 m s^{-1} (with a large variance) under the melting layer (Figs. 6b,d); liquid precipitation generally has a larger fall velocity than solid precipitation. The Doppler velocity gradually increases from top to bottom across the height ranges of the melting layer. This velocity structure indicates the existence of a gradual transition of the dominant phase, that is, from solid ice particles to liquid droplets through the intermediate state. The small fall velocity in the melting layer causes delay in the particle falling and consequently a relative increase in the particle number concentration when compared with that underneath the layer. This effect may contribute to a relative increase in radar reflectivity in combination with a change of particle dielectric properties by melting.

Figure 7 contains the panels showing normalized contoured-frequency-by-temperature diagrams (CFTDs) and the averaged values on the temperature axis for the MRR measurements. These plots highlight the relation between the brightband structure and the temperature profile. Because no vertical sounding data were obtained at the Jarvenpaa site on the dates, the temperature profiles at the Jokioinen site (Fig. 3) were substituted. The Jokioinen temperature data were vertically and temporally interpolated on the MRR data grids to plot the CFTDs. Note that this approach may lead to an artificial expansion of the bright band on the temperature axis because of the disagreement between the actual and substitute temperature profiles.

The CFTDs of the observed reflectivity (Figs. 7a,i) show relatively large reflectivities from $\sim 0^\circ$ to 3°C on the case-study days. These features can also be confirmed in the line graphs for the averaged values (Figs. 7d,l). This result suggests that the temperature profile obtained at the Jokioinen site works reasonably well as a substitute to plot the CFTDs. The mean Doppler velocity also gradually increases in the temperature range from 0° to 3°C (Figs. 7e,m).

Figures 7b, 7f, 7j, and 7n illustrate the corresponding CFTDs of Z_{ew} and v_d derived from the WRF-SBM simulations using the time-dependent melting scheme. Here, $|K^2|$ was set at 0.92 to calculate Z_{ew} for compatibility. The CFTDs were plotted using the sampled values of all model grid columns in domain 3, except for the edges of the domain, large-surface-rainfall (over 1 mm h^{-1}) grids, and grids with very little or no rainfall (less than 0.1 mm h^{-1}); the aim of the filtering process was to sample only vertical columns having surface

rainfall rates that are similar to the values obtained at the Jarvenpaa site (Fig. 2). Temperature, Z_{ew} , and v_d were interpolated at vertical levels every 100 m.

The simulation CFTDs (Figs. 7b,f,j,n) and line graphs (Figs. 7d,h,l,p) share some common characteristics with the observation ones, especially in terms of the profiles within the melting layers: Increases in reflectivity appear at the temperature ranges from approximately 0° to 3°C . The peaks in the mean reflectivity are located at 2°C in the measurements and at 1.5°C in the simulation results. The differences between the peak values of the averaged reflectivity and the values at 0°C are approximately 5 dBZ in the measurements and 3 dBZ in the simulation results. The mean Doppler velocity gradually increases with temperature in the range from 0° to 3°C in both measurements and simulations. However, the simulation significantly overestimates the reflectivity in the entire temperature range as well as the Doppler velocity in most of the temperature range greater than 0°C . Overestimation of radar reflectivity is common to the comparisons with these MRR measurements and the C-band 3D radar measurements in section 3b.

The overall overestimation of the reflectivity and the Doppler velocity indicates a possibility that the particle sizes are generally overestimated. This can be justified by evaluating the surface drop size distribution (DSD) by comparison with ground-based disdrometer measurements. Figures 8a and 8b illustrate the mean surface DSDs obtained from the two types of disdrometer measurements and the simulations; the surface DSDs are averaged over all samples with surface rain rates between 0.5 and 1.0 mm h^{-1} . DSD profiles corresponding to both types of disdrometers are similar for both dates. The measured DSDs have peaks within the plotted axis ranges, whereas the simulated number density monotonically decreases with diameter (although the graph shows the number density range only at less than $1000 \text{ m}^{-3} \text{ mm}^{-1}$). This difference is due to a deficiency in the capability of the disdrometers to detect tiny droplets (Tokay et al. 2001, 2005). In the diameter range that is larger than approximately 1.5 mm, the simulation overestimates the number density. The measured maximum diameters are roughly 2.0 mm by the 2DVD and 2.5 mm by the Parsivel disdrometer under the condition that the minimum detection limit for the number density is approximately $0.01 \text{ m}^{-3} \text{ mm}^{-1}$; the corresponding diameters in the simulations are roughly 3.7 mm.

The overestimation of the number density at large diameter ranges is consistent with the overestimation of the Doppler velocity at temperatures over 4°C : The simulated maximum velocity estimated from the CFTDs (Figs. 7f,n) is roughly 8 m s^{-1} ; a terminal fall velocity of 8 m s^{-1} corresponds to a droplet of roughly 3 mm in

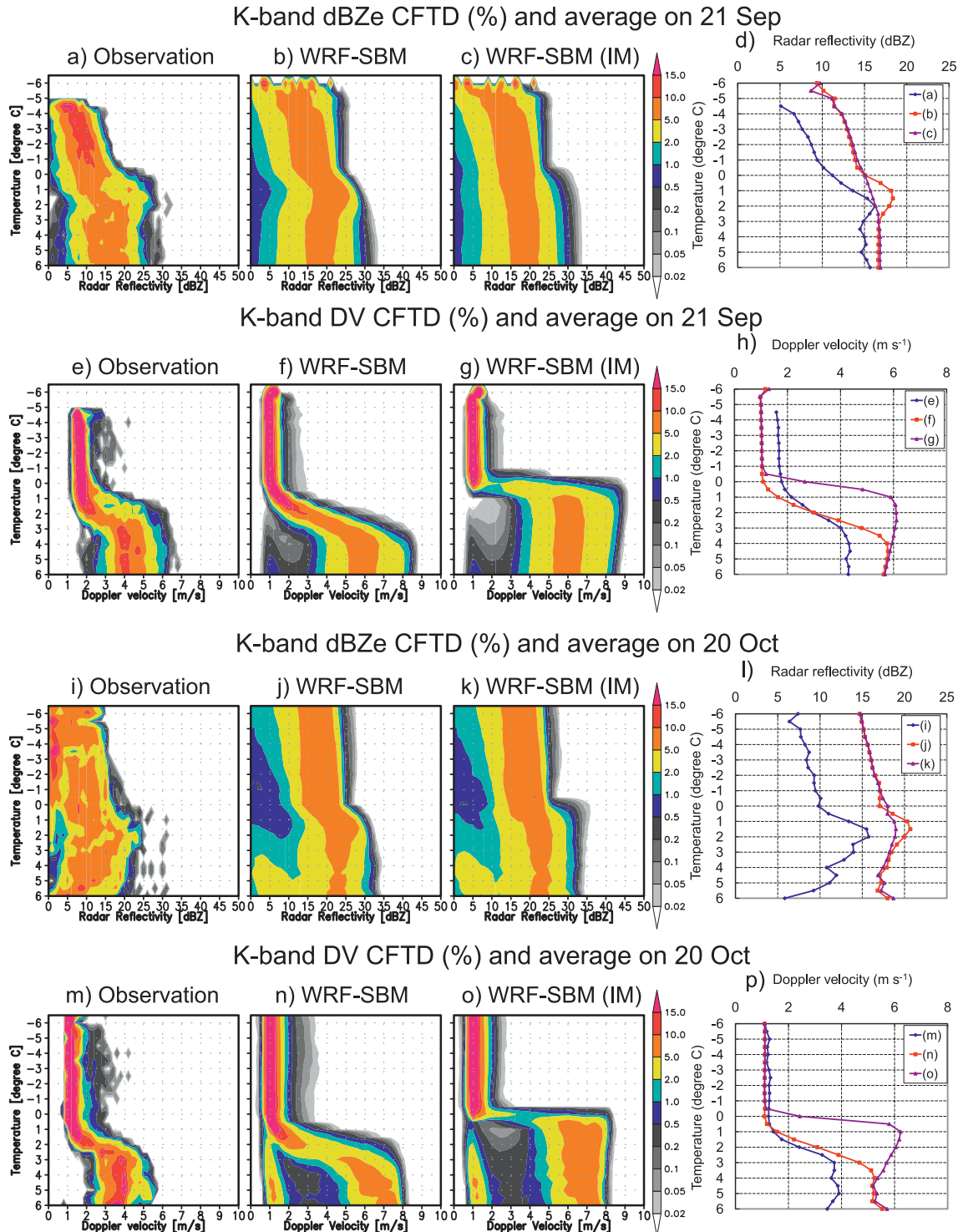


FIG. 7. CFTDs of the water equivalent radar reflectivity factor (dBZ) derived from the MRR measurements at the Jarvenpaa site coupled with the vertical temperature profiles of sounding data at the Jokioinen site and obtained from the WRF-SBM simulations in the 21 Sep case: (a) the measurements, (b) WRF-SBM simulation using the time-dependent melting scheme, and (c) simulation using the instantaneous melting scheme; (i)–(k) as in (a)–(c), but in the 20 Oct case. CFTDs of the mean Doppler velocity (m s^{-1}): (e) the measurements, (f) WRF-SBM simulation using the time-dependent melting scheme, and (g) simulation using the instantaneous melting scheme; (m)–(o) as in (e)–(g), but for the 20 Oct case. (right) Profiles of (d) averaged water equivalent radar reflectivity factor (dBZ) and (h) averaged mean Doppler velocity (m s^{-1}) on temperature from the CFTDs in the 21 Sep case; (l), (p) as in (d) and (h), but for the 20 Oct case.

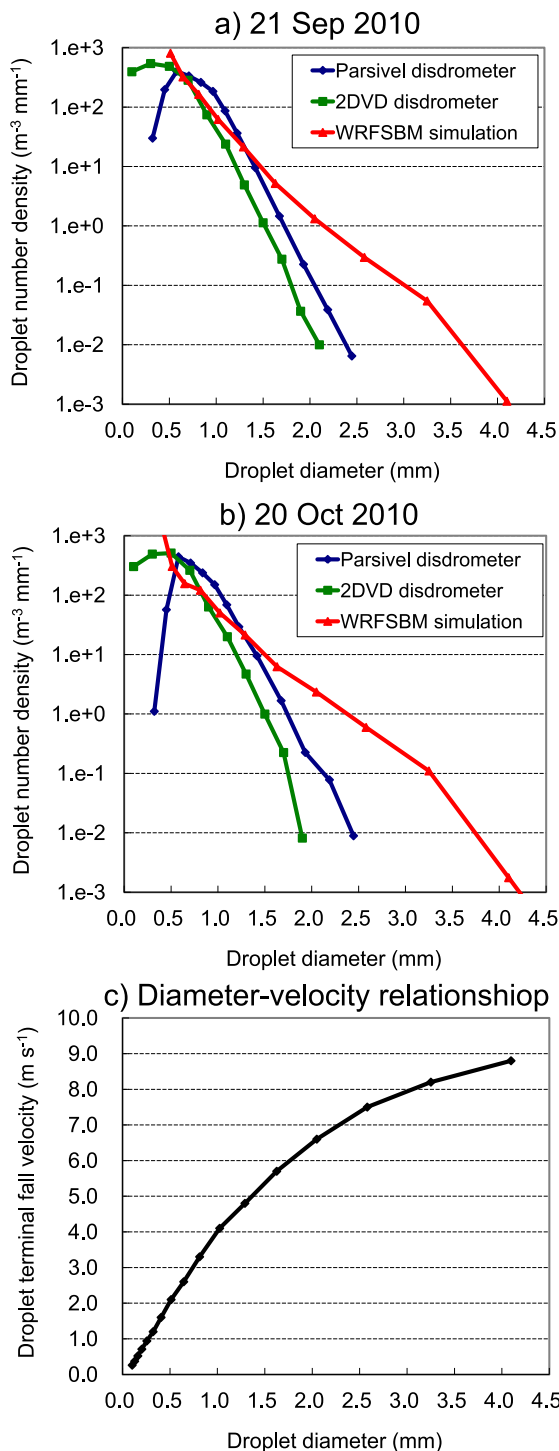


FIG. 8. Surface DSDs in the form of number concentration density distribution ($\text{m}^{-3} \text{mm}^{-1}$) averaged within the surface rainfall-rate range from 0.5 to 1 mm h^{-1} obtained from the Parsivel disdrometer and 2DVD measurements at Jarvenpaa site and the WRF-SBM simulation on (a) 21 Sep and (b) 20 Oct. (c) Relation between the terminal fall velocity (m s^{-1}) at 1000 hPa and the droplet diameter (mm), used in the WRF-SBM microphysical scheme.

diameter (Fig. 8c). The simulated number density at 3-mm diameter is about $0.1 \text{ m}^{-3} \text{mm}^{-1}$. In contrast, a number density of $0.1 \text{ m}^{-3} \text{mm}^{-1}$ is observed for 2-mm diameter droplets with a corresponding terminal fall velocity of roughly 6 m s^{-1} . This velocity is generally in agreement with the maximum Doppler velocity in the observation CFTDs (Figs. 7e,m).

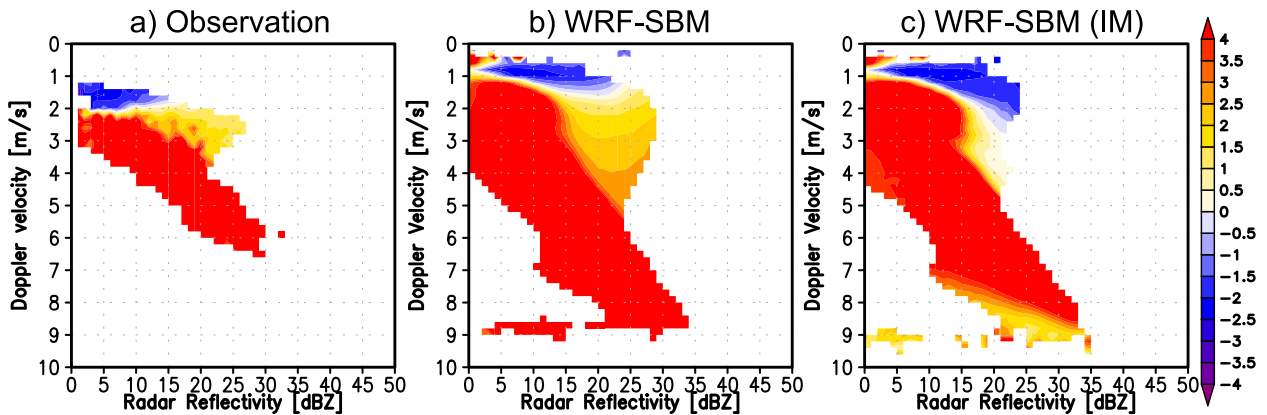
Figures 7c and 7k illustrate the corresponding reflectivity CFTDs derived from the simulations using the instantaneous melting scheme. The profiles are different from those of the default simulations using the time-dependent melting scheme (Figs. 7b,j). A bias toward the large-reflectivity side in the high-probability part in the temperature range of 0° – 3°C does not appear in the CFTDs. The mean reflectivity profile in Fig. 7d shows no peak in the temperature range. Although there is a peak in the profile in Fig. 7l, the difference from the value at 0°C is approximately only 1 dBZ, which is smaller than those in the observations and the default simulation profiles.

The structure of the mean Doppler velocity in the melting layer is also different between the two types of simulations. The CFTDs (Figs. 7g,o) of the simulations using the instantaneous melting scheme have no gradual zone of velocity change as compared with the observations and the default simulation diagrams. The averaged velocity profiles around the bright bands in the simulations using the instantaneous melting scheme are very different from those in the observation and the default simulation profiles (Figs. 7h,p). The artificial peaks in the averaged velocity are centered at 2°C on 21 September and at 1°C on 20 October.

To highlight the dependence of the correlation between radar reflectivity and Doppler velocity on temperature, Fig. 9 shows contoured temperature diagrams for both parameters (e.g., Yuter and Houze 1995). The color contour shows the mean temperature in samples having values in the particular reflectivities and Doppler velocity ranges. From the measurements (Figs. 9a,d), most of the area having temperatures of less than 0°C is biased to the upper-left side of the plot domain; this is because ice cloud and precipitation have relatively small reflectivity and velocity. Bright bands are identified as the region with temperatures from approximately 0° to 3°C with a relatively small velocity of less than 3 m s^{-1} but large reflectivity up to 25 dBZ. Liquid cloud and precipitation not including melting particles corresponds to the temperature area greater than 4°C . The temperature area occupies most of the part with velocity larger than 3 m s^{-1} . These characteristics are generally common in the diagrams of the two cases.

Figures 9b and 9e show the corresponding diagrams derived from the simulation results using the time-dependent

K-band contoured temperature diagram (degree C) on 21 Sep



K-band contoured temperature diagram (degree C) on 20 Oct

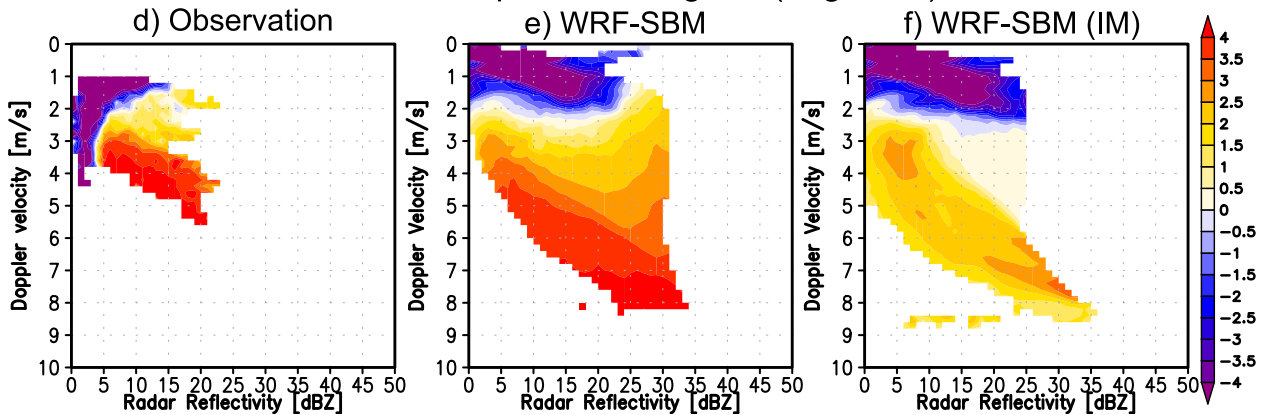


FIG. 9. Contoured averaged-temperature diagram for the water equivalent radar reflectivity factor (dBZ) and the mean Doppler velocity (m s^{-1}) derived from the MRR measurements and the WRF-SBM simulations. The color contour shows the temperature averaged in samples in the 1-dBZ reflectivity and 0.1 m s^{-1} Doppler velocity intervals.

melting scheme. The area with temperatures below 0°C is distributed on the upper side of the plot domain. The area with temperatures ranging from approximately 0° to 3°C is mostly located at the periphery of the lower-right side of the freezing-temperature part. The area extends toward the large-reflectivity side of the plot because of brightband effects. This is an important characteristic in common with the observation and the simulation diagrams. In contrast, a different behavior is shown in the corresponding diagrams of the simulations using the instantaneous melting scheme (Figs. 9c,f). The difference between the diagrams of the different simulations highlights the effects of the time-dependent melting process. As compared with the default simulations (Figs. 9b,e), the region from approximately 0° to 3°C on the right periphery is almost absent in Figs. 9c and 9f. Thus, the corresponding part in the default-simulation diagram is identified as being due to the brightband effect, because

the simulations using the instantaneous melting scheme do not represent it. This comparative result in Fig. 9 suggests that the model using the time-dependent melting scheme has clearly provided a better simulation of the bright bands than does the model using the instantaneous melting scheme.

2) SENSITIVITY OF LIQUID WATER FRACTION ON TEMPERATURE AND PARTICLE SIZE VARIATIONS

The liquid mass fraction of a melting particle is an important parameter to determine the fall velocity and the dielectric parameter related to the radar reflectivity. One of the great advantages of SBM is being able to calculate and represent the behavior of the melting process individually for different particle sizes. This function is of significant importance in calculating the brightband reflectivity. The backscattering efficiency of

a melting particle has a nonlinear change according to the particle size, the liquid water fraction, and the radar transmitted frequency (see the [appendix](#)).

Figure 10 shows the dependence of two parameters that are related to the liquid water fraction of melting particles on temperature in the simulations using the time-dependent melting scheme. The simulation results within and around the melting layer were sampled to show the mean statistical relationship between the ambient air temperature and the liquid water fraction of melting particles in different particle size bins. We employed the same sampling filter according to the surface rainfall rate as was used in the comparison with the MRR measurements.

The first parameter is the mass ratio of the liquid water content (the total mass of liquid droplets and liquid parts in melting snow, graupel and hail) to the total water content of all hydrometeors (LFT):

$$\text{LFT} = \frac{(g_{\text{dw}} + g_{\text{sw}} + g_{\text{gw}} + g_{\text{hw}})}{g_{\text{all}}}, \quad (7)$$

where g is the mass concentration; the subscripts dw, sw, gw, hw, and all denote the variables of liquid droplets, liquid parts in melting snow aggregates, graupel and hail, and all hydrometeors in total, respectively. If LFT is unity, all hydrometeors exist in the liquid phase. If LFT is zero, all hydrometeors exist in the solid phase without melting.

The second parameter is the mass-averaged liquid fraction in melting snow aggregates (LFS), which is defined as the ratio of the liquid mass in melting snow aggregates to the total mass of unmelted and melted snow aggregates:

$$\text{LFS} = \frac{g_{\text{sw}}}{g_{\text{sw}} + g_{\text{si}}}, \quad (8)$$

where the subscript si denotes the solid (ice) part of snow aggregates. Note that completely melted snow aggregates are not counted because they are already converted into the category of liquid droplets. If the values of LFT and LFS are identical, the melting snow aggregates that have the liquid mass fraction of the value of LFS dominate. These two parameters have been calculated separately for each of the three mass bins in the SBM to show the particle size dependence. The subscripts of the captions (100, 500, and 1000) in Fig. 10 denote the parameters of the size bins that have equivalent liquid droplet radii—approximately 100, 500, and 1000 μm , respectively. We discuss the liquid water fractions of snow aggregates only, because there are few amounts of graupel and hail in the case-study simulations.

Figure 10 shows that LFT_100 increases from approximately 0.85 or 0.9 to 1 in temperature ranges from

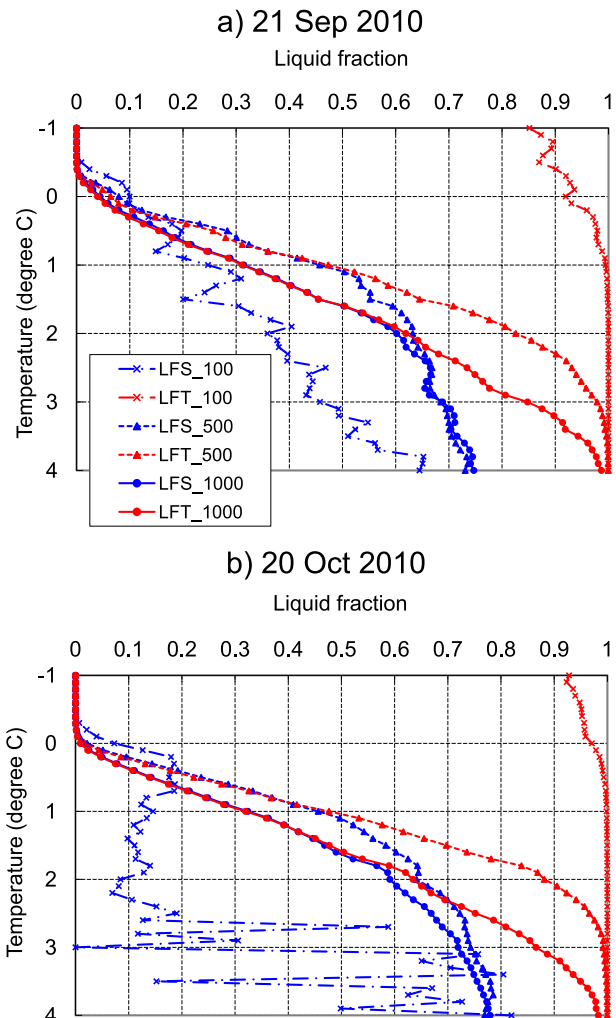


FIG. 10. Profiles of the LFT and LFS parameters related to liquid water fractions on temperature in the WRF-SBM simulations for the cases of (a) 21 Sep and (b) 20 Oct. LFT is the parameter defined as the mass ratio of the liquid water content (the total of liquid droplets and liquid masses in melting snow aggregates, graupel, and hail) to the total water content of all hydrometeors. LFS is defined as the mass-averaged liquid fraction of melting snow aggregates. The subscripts of the figure label, 100, 500, and 1000, denote the particle radii of equivalent droplet mass bins: approximately 100 μm , 500 μm , and 1 mm, respectively.

–1° to 1°C and becomes constant at temperatures of larger than 1°C. The LFT is close to 1 even at temperatures less than 0°C, which means that very few ice particles of that size exist around the melting layer. Few ice particles of this size fall to the melting layer, probably because most ice particles grow beyond this size at higher vertical levels. LFS_100 is meaningless because of the absence of snow aggregates of this size.

In contrast, LFT_500 and LFT_1000 are almost zero at temperatures of less than 0°C and gradually increase

with temperature, reaching unity at approximately 4°C. LFT_500 reaches unity at a lower temperature than LFT_1000 does, since the particles with smaller fall velocities and masses melt at a higher vertical level, that is, lower temperature. The values of LFT_1000 and LFS_1000 are identical until approximately 2°C, whereas LFT_500 and LFS_500 are identical until 1°C and have different values at 2°C. Since the agreement between LFT and LFS values means predominance of melting snow aggregates whose liquid water fraction is the value of LFS, this result suggests that larger snow aggregates are more likely to stay partly melted before completely melting.

If LFT is larger than LFS and less than unity, it means that liquid droplets exist together with melting snow aggregates. The LFS_500 and LFS_1000 do not converge to unity even when LFT_500 and LFT_1000 are close to unity. This behavior indicates that a sudden conversion from melting snow aggregates to liquid droplets occurs. The threshold value of the liquid water fraction for the conversion is estimated to be roughly from 0.5 to 0.75 for LFS_500 and from 0.6 to 0.75 for LFS_1000. Values on the order of 0.8–0.9 are not properly simulated, probably because the present time step and vertical grid intervals are not enough to resolve them.

There is no significant influence on the reflectivity simulation at the K-band frequency of the missing liquid fractions on the order of 0.8–0.9 by the sudden conversion from melting snow aggregates to liquid droplets. This is because a particle with a liquid water fraction of unity, that is, a liquid droplet, has the largest backscattering efficiency in the range of the fraction from 0 to 1 in the MG2 model at 24.15 GHz for any of the three particle sizes (appendix Fig. A1). Note that the MG2 model is now applied to the calculation of scattering properties of melting snow aggregates. If the MG1 or EM model is applied to the calculation, however, melting snow aggregates with a particular liquid fraction have larger backscattering efficiency than liquid droplets. Thus, the failure to resolve large liquid water fractions may cause underestimation of brightband reflectivity in the melting layer.

The simulated K-band reflectivity shows relative increases of reflectivity in the melting layer (Fig. 7). Since melting snow aggregates have a backscattering efficiency that is less than those of liquid droplets with the same sizes in the MG2 model at K band (appendix Fig. A1), the change of dielectric properties by melting cannot solely cause the increases of reflectivity. Thus another factor, the effect of a particle falling slowly through the melting layer, may substantially increase the reflectivity. The small Doppler velocity is linked to

the large reflectivity in the melting layer (Fig. 9); this characteristic is common between the observations and simulations.

4. Summary and conclusions

In this paper, we conducted case-study simulations using the WRF–SBM for reproducing two mixed-phase precipitation events during the LPVEx field campaign. The SBM has a function to represent a realistic melting process from solid to liquid particles by predicting the liquid water fraction of melting particles. The simulation results were compared with the C-band 3D radar and vertically pointing K-band radar measurements for the rainfall events. The radar signatures containing bright bands were explicitly simulated through a straightforward reflectivity calculation using the WRF–SBM output.

The simulated profiles of cloud and precipitation were evaluated by comparison with the C-band 3D radar measurements. The coverage of the observed cloud and precipitation was simulated reasonably well in the 21 September case, whereas some forecast displacement errors were highlighted in the 20 October case. Overall, overestimation of the reflectivity and the existence of artificial convective clouds were common problems in both cases. The reflectivity overestimation was related to the bias of PSD toward larger particle sizes, which was evaluated through a comparison with the surface DSD of the ground-based disdrometer measurements.

The comparison with the C-band 3D radar measurements highlighted some errors that are due to a shortage of functionality in the radar simulator that was used here. The simulated 3D field of reflectivity was composed of vertically pointing signals spread over the horizontal domain, in place of the strict reflectivity calculation of the radar signal reflected by the target and received by the radar system. This deficiency in the present simulator caused an artificial overestimation of reflectivity at the brightband heights that was due to a lack of more advanced analysis of the comparison of parameters such as polarimetric moments and ZDR. Additional development of the radar simulator is necessary for further insight into the microphysical structure acquired from radar measurements.

Detailed discussion about the simulated brightband structure was obtained from comparisons with the vertically pointing K-band radar measurements. Weak bright bands were observed in the reflectivity signatures, and the characteristics were reproduced reasonably well in the simulations. The bright bands were distributed in the air temperature range from approximately 0° to 3°C. An increase in reflectivity and a gradual change of Doppler velocity were simultaneously observed and

simulated in the temperature range. The effectiveness of the time-dependent melting scheme to reproduce bright bands was verified through intercomparison with the corresponding simulations using the contrasting instantaneous melting scheme. The new time-dependent melting scheme has some shortcomings, however. There was artificial discontinuous conversion from melting snow aggregates to completely melted droplets. The state with a high liquid water fraction on the order of 80%–90% was not able to be resolved under the employed time step and vertical resolution. This numerical shortcoming may result in underestimation of bright-band reflectivity in melting layers according to the assumption about the melting-particle structure.

In this study, the melting-layer structure in the 3D simulation using fully explicit SBM was indirectly evaluated through the analysis of the bright bands in the radar signatures. Direct validation of the simulated melting process is an important subject for further evaluation. There is significant uncertainty in the modeling of microphysical processes of melting particles, for example, in terms of the melting-particle structure largely related to the changes of melting fraction, particle temperature, and evaporation/sublimation rates. The changes of particle shape, density, and fall velocity during melting are also not well known. The aircraft in situ measurements of [Heymsfield and Aaron \(2013\)](#) qualitatively showed that melting particles mostly existed in the temperature range from 0° to 2°C in mixed-phase clouds during the LPVEx field campaign. The result suggested a possibility of a slower melting process in the present model. On the other hand, [Misumi et al. \(2014\)](#) reported direct measurements of liquid water fractions on ground level. Large liquid fractions in melting particles were observed even at low temperature; for example, the averaged water fraction at 1°C was approximately 80% in certain environments. This result also suggested a possibility of a delay in the melting process in the present model. The coupling of these new observational data and our simulator-based approach will shed a new light of better understanding and improvement of the melting process in atmospheric models in future study.

Acknowledgments. This study was supported by the NASA GPM Ground Validation program (Dr. Mathew R. Schwaller). The sounding data at the Jokioinen site were kindly provided by the Department of Atmospheric Science of the College of Engineering at the University of Wyoming. The authors thank the two anonymous reviewers for their comments in improving the manuscript. This paper is dedicated to the memory of Arthur Y. Hou.

APPENDIX

Sensitivity of Backscattering Efficiency to Melting-Structure Model, Particle Size, and LWF

As described in [section 2c](#), the G-SDSU has several assumptions in the modeling of the melting-particle structure for the calculation of the effective dielectric properties. The main part of this paper has provided a discussion that is based on the simulation result using only the specific options in which the assumptions are most consistent with those in the WRF-SBM microphysics. This appendix introduces the sensitivity of the backscattering efficiency to selection of the available options in the radar simulator.

[Figure A1](#) illustrates the dependence of the backscattering efficiency at 5.65 GHz (C band) and 24.15 GHz (K band) on the liquid water fraction of melting snow aggregates in the three particle size bins with equivalent liquid droplet radii of 100, 500, and 1000 μm . The following three types of the particle structure model have been used to calculate the effective dielectric properties: 1) MG1, which is the Maxwell Garnett function with the ice-inclusion and water-matrix assumptions, 2) MG2, which is the Maxwell Garnett function with the water-inclusion and ice-matrix assumptions, and 3) EM, which is the effective-medium function with the homogenous mixing assumption. The riming effect is not considered in this calculation since the LPVEx simulations have little of the supercooled water that causes riming of snow aggregates.

[Figure A1a](#) shows the relation between the backscattering efficiency at 5.65 GHz and the liquid water fraction of the snow aggregate (the equivalent droplet radius is 100 μm). The backscattering efficiency of the MG2 model monotonically increases with liquid water fraction. The functions of the MG1 and EM models have peaks at certain liquid fractions of less than 1; the peaks appear at approximately 0.45 and 0.65 of the liquid fractions in the MG1 and EM functions. The MG1 model has the largest backscattering efficiency among these models at any liquid fraction. The EM model has the smallest value at a low liquid fraction of less than 0.4; the value at a high liquid fraction over 0.4 is larger than that of MG2, and the function eventually converges on that of MG1. In [Fig. A1b](#) (500- μm equivalent droplet radius), the MG2 function has a slight peak of the backscattering efficiency at a liquid fraction of approximately 0.8. The MG1 and EM functions have peaks at liquid fractions of approximately 0.5 and 0.8, respectively, which are larger than the peak fractions in the particle size of 100 μm ([Fig. A1a](#)). For the 1000- μm equivalent droplet radius ([Fig. A1c](#)), the functions of the models are very similar to those in [Fig. A1b](#). The peaks

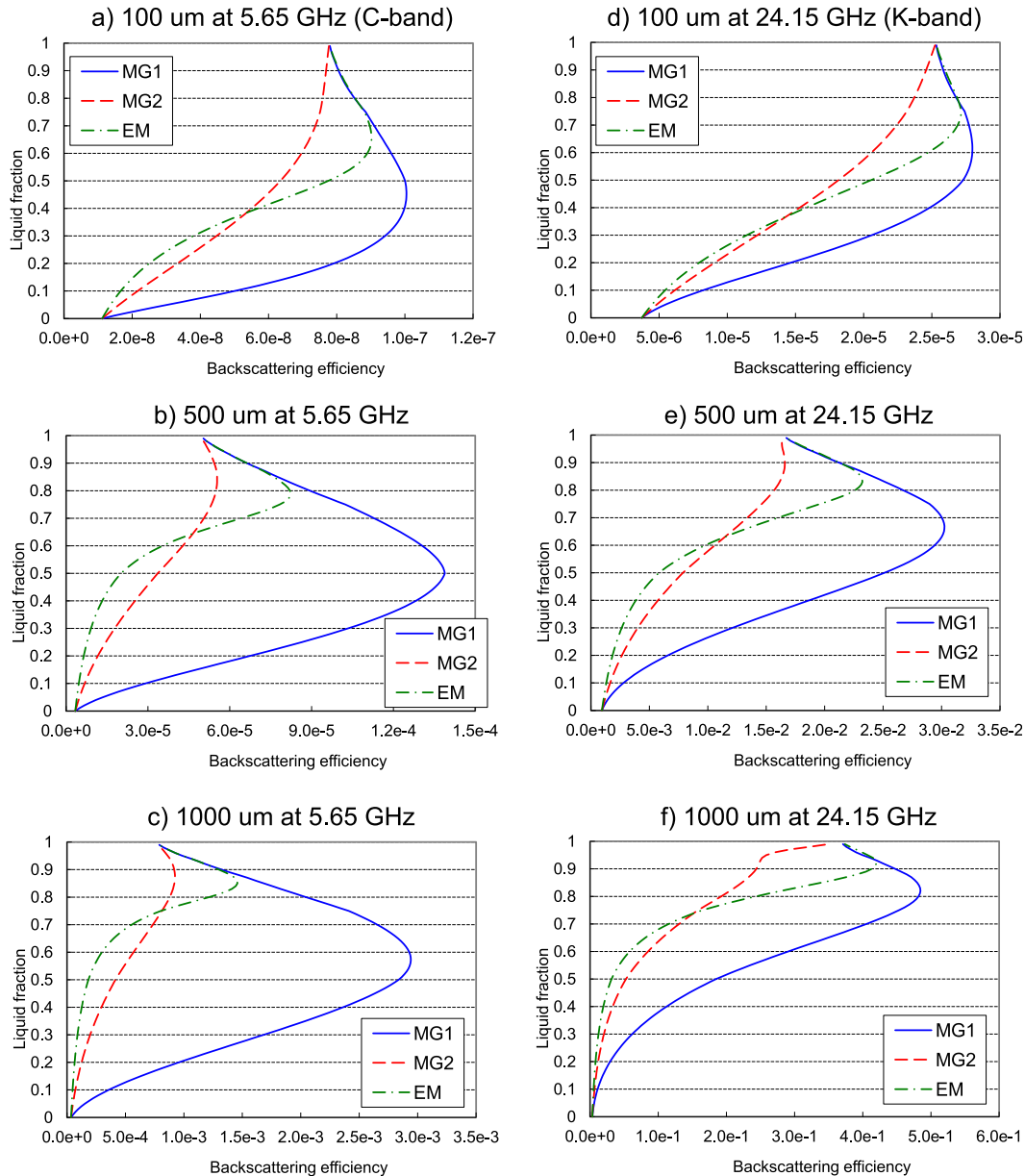


FIG. A1. Relation between the backscattering efficiency and the liquid water fraction in melting snow aggregates at (left) 5.65 GHz (C band) and (right) 24.15 GHz (K band) radar frequencies in the radar simulator. The MG1, MG2, and EM abbreviations are defined in the text. The indices of the particle sizes—100, 500, and 1000 μm —show the particle radii of equivalent droplet mass bins.

of the backscattering efficiencies are at liquid fractions of 0.55, 0.85, and 0.85 in the MG1, MG2, and EM models; these peak fractions are larger than those in the particle sizes of 100 and 500 μm .

Figures A1d, A1e, and A1f show the same graphs as Figs. A1a, A1b, and A1c, but at 24.15 GHz (K band). The characteristics of the functions are generally similar to those at 5.65 GHz except for the following points: The function of the 1000- μm MG2 model (Fig. A1f) has no

peak. The function of the 500- μm MG2 model (Fig. A1e) has a small peak, but the peak backscattering efficiency is almost equivalent to that at a liquid fraction of unity, that is, that of a corresponding liquid droplet. The functions of the MG1 and EM models have their peaks at high liquid fractions relative to those at 5.65 GHz. For example, the peak liquid fractions in Fig. A1f are approximately 0.8 in the MG1 model and 0.9 in the EM model; these peak fractions are larger than those in Fig. A1c.

Overall, the MG1 model provides the largest backscattering efficiency of the structure models across the plotted particle size and the liquid-fraction ranges. The EM model has the smallest efficiency at a low liquid fraction, but the function becomes closer to that of the MG1 model at a high liquid fraction. There are peaks of the backscattering efficiency at a certain liquid fraction of less than 1 in the functions of the MG1 and EM models, and the peak liquid fractions increase with particle size. On the other hand, the value of MG2 is at a maximum at a liquid fraction of unity at K-band frequency, whereas peaks appear in the C-band plots except for the case of 100- μm equivalent droplet radius (Fig. A1a).

REFERENCES

- Atlas, D., R. C. Srivastava, and R. S. Sekon, 1973: Doppler radar characteristics of precipitation at vertical incidence. *Rev. Geophys. Space Phys.*, **11**, 1–35, doi:10.1029/RG011i001p00001.
- Austin, P. M., and A. C. Bemis, 1950: A quantitative study of the “bright band” in radar precipitation echoes. *J. Meteor.*, **7**, 145–151, doi:10.1175/1520-0469(1950)007<0145:AQSOTB>2.0.CO;2.
- Bauer, P., J. P. V. Poiares Baptista, and M. de Iulius, 1999: On the effect of the melting layer on the microwave emission of clouds over the ocean. *J. Atmos. Sci.*, **56**, 852–867, doi:10.1175/1520-0469(1999)056<0852:TEOTML>2.0.CO;2.
- , A. Khain, A. Pokrovsky, R. Meneghini, C. Kummerow, F. Marzano, and J. P. V. Poiares Baptista, 2000: Combined cloud–microwave radiative transfer modeling of stratiform rainfall. *J. Atmos. Sci.*, **57**, 1082–1104, doi:10.1175/1520-0469(2000)057<1082:CCMRTM>2.0.CO;2.
- Bohren, C. F., and L. J. Battan, 1980: Radar backscattering by inhomogeneous precipitation particles. *J. Atmos. Sci.*, **37**, 1821–1827, doi:10.1175/1520-0469(1980)037<1821:RBBIPP>2.0.CO;2.
- , and —, 1982: Radar backscattering of microwaves by spongy ice spheres. *J. Atmos. Sci.*, **39**, 2623–2629, doi:10.1175/1520-0469(1982)039<2623:RBOMBS>2.0.CO;2.
- Dabberdt, W., J. Koistinen, J. Poutiainen, E. Saltikoff, and H. Turtiainen, 2005: The Helsinki Mesoscale Testbed: An invitation to use a new 3-D observation network. *Bull. Amer. Meteor. Soc.*, **86**, 906–907, doi:10.1175/BAMS-86-7-906.
- Dee, D. P., and Coauthors, 2011: The ERA-Interim reanalysis: Configuration and performance of the data assimilation system. *Quart. J. Roy. Meteor. Soc.*, **137**, 553–597, doi:10.1002/qj.828.
- Dudhia, J., 1989: Numerical study of convection observed during the Winter Monsoon Experiment using a mesoscale two-dimensional model. *J. Atmos. Sci.*, **46**, 3077–3107, doi:10.1175/1520-0469(1989)046<3077:NSOCOD>2.0.CO;2.
- Fabry, F., and I. Zawadzki, 1995: Long-term radar observations of the melting layer of precipitation and their interpretation. *J. Atmos. Sci.*, **52**, 838–851, doi:10.1175/1520-0469(1995)052<0838:LTROOT>2.0.CO;2.
- , and W. Szyrmer, 1999: Modeling of the melting layer. Part II: Electromagnetic. *J. Atmos. Sci.*, **56**, 3593–3600, doi:10.1175/1520-0469(1999)056<3593:MOTMLP>2.0.CO;2.
- Gallus, W. A., Jr., and M. Pfeifer, 2008: Intercomparison of simulations using 5 WRF microphysical schemes with dual-polarization data for a German squall line. *Adv. Geosci.*, **16**, 109–116, doi:10.5194/adgeo-16-109-2008.
- Grell, G. A., and D. Devenyi, 2002: A generalized approach to parameterizing convection combining ensemble and data assimilation techniques. *Geophys. Res. Lett.*, **29**, 1693, doi:10.1029/2002GL015311.
- Heffernan, E., and J. Marwitz, 1996: The Front Range blizzard of 1990. Part II: Melting effect in a convective band. *Mon. Wea. Rev.*, **124**, 2469–2482, doi:10.1175/1520-0493(1996)124<2469:TFRBOP>2.0.CO;2.
- Heymsfield, A., and B. Aaron, 2013: Properties of ice cloud and melting layer from LPVEx, MC3E and GCPEX. *2013 PMM Science Team Meeting*, Annapolis, MD, NASA.
- Hou, A. Y., and Coauthors, 2014: The Global Precipitation Measurement (GPM) mission. *Bull. Amer. Meteor. Soc.*, **95**, 701–722, doi:10.1175/BAMS-D-13-00164.1.
- Iguchi, T., T. Nakajima, A. P. Khain, K. Saito, T. Takemura, H. Okamoto, T. Nishizawa, and W.-K. Tao, 2012a: Evaluation of cloud microphysics in JMA-NHM simulations using bin or bulk microphysical schemes through comparison with cloud radar observations. *J. Atmos. Sci.*, **69**, 2566–2586, doi:10.1175/JAS-D-11-0213.1.
- , and Coauthors, 2012b: Numerical analysis using WRF-SBM for the cloud microphysical structures in the C3VP field campaign: Impacts of supercooled droplets and resultant riming on snow microphysics. *J. Geophys. Res.*, **117**, D23206, doi:10.1029/2012JD018101.
- Janjić, Z. I., 1990: The step-mountain coordinate: Physical package. *Mon. Wea. Rev.*, **118**, 1429–1443, doi:10.1175/1520-0493(1990)118<1429:TSMCPP>2.0.CO;2.
- Khain, A., B. Lynn, and J. Dudhia, 2010: Aerosol effects on intensity of landfalling hurricanes as seen from simulations with the WRF Model with spectral bin microphysics. *J. Atmos. Sci.*, **67**, 365–384, doi:10.1175/2009JAS3210.1.
- , A. Pokrovsky, D. Rosenfeld, U. Blahak, and A. Ryzhkov, 2011: The role of CCN in precipitation and hail in a mid-latitude storm as seen in simulations using a spectral (bin) microphysics model in a 2D dynamic frame. *Atmos. Res.*, **99**, 129–146, doi:10.1016/j.atmosres.2010.09.015.
- , V. Phillips, N. Benmoshe, and A. Pokrovsky, 2012: The role of small soluble aerosols in the microphysics of deep maritime clouds. *J. Atmos. Sci.*, **69**, 2787–2807, doi:10.1175/2011JAS3649.1.
- Klaassen, W., 1988: Radar observations and simulation of the melting layer of precipitation. *J. Atmos. Sci.*, **45**, 3741–3753, doi:10.1175/1520-0469(1988)045<3741:ROASOT>2.0.CO;2.
- Köhler, H., 1936: The nucleus in and the growth of hygroscopic droplets. *Trans. Faraday Soc.*, **32**, 1152–1161, doi:10.1039/tf9363201152.
- Lang, S., W.-K. Tao, R. Cifelli, W. Olson, J. Halverson, S. Rutledge, and J. Simpson, 2007: Improving simulations of convective systems from TRMM LBA: Easterly and westerly regimes. *J. Atmos. Sci.*, **64**, 1141–1164, doi:10.1175/JAS3879.1.
- L’Ecuyer, T., W. Petersen, and D. Moiseev, 2010: Light Precipitation Validation Experiment (LPVEx). LPVEx Science Plan (6/7/10 draft), 29 pp. [Available online at http://lpvex.atmos.colostate.edu/docs/lpvex_science_plan_June2010.pdf.]
- Löffler-Mang, M., and J. Joss, 2000: An optical disdrometer for measuring size and velocity of hydrometeors. *J. Atmos. Oceanic Technol.*, **17**, 130–139, doi:10.1175/1520-0426(2000)017<0130:AODFMS>2.0.CO;2.
- Masunaga, H., and C. D. Kummerow, 2005: Combined radar and radiometer analysis of precipitation profiles for a parametric retrieval algorithm. *J. Atmos. Oceanic Technol.*, **22**, 909–929, doi:10.1175/JTECH1751.1.

- Matrosov, S. Y., 2008: Assessment of radar signal attenuation caused by the melting hydrometeor layer. *IEEE Trans. Geosci. Remote Sens.*, **46**, 1039–1047, doi:10.1109/TGRS.2008.915757.
- Matsui, T., X. Zeng, W.-K. Tao, H. Masunaga, W. Olson, and S. Lang, 2009: Evaluation of long-term cloud-resolving model simulations using satellite radiance observations and multi-frequency satellite simulators. *J. Atmos. Oceanic Technol.*, **26**, 1261–1274, doi:10.1175/2008JTECHA1168.1.
- , and Coauthors, 2013: GPM satellite simulator over ground validation sites. *Bull. Amer. Meteor. Soc.*, **94**, 1653–1660, doi:10.1175/BAMS-D-12-00160.1.
- Maxwell Garnett, J. C., 1904: Colours in metal glasses and in metallic films. *Philos. Trans. Roy. Soc. London*, **203A**, 385–420, doi:10.1098/rsta.1904.0024.
- METEK, 2009: MRR physical basics, version 5.2.0.1. METEK GmbH Manual, 20 pp. [Available online at http://www2.meteo.uni-bonn.de/mitarbeiter/stroemel/doku.php/meteorological_laboratory.]
- Misumi, R., H. Motoyoshi, S. Yamaguchi, S. Nakai, M. Ishizaka, and Y. Fujiyoshi, 2014: Empirical relationships for estimating liquid water fraction of melting snowflakes. *J. Appl. Meteor. Climatol.*, **53**, 2232–2245, doi:10.1175/JAMC-D-13-0169.1.
- Mitra, S. K., O. Vohl, M. Ahr, and H. R. Pruppacher, 1990: A wind tunnel and theoretical study of the melting behavior of atmospheric ice particles. Part IV: Experiment and theory for snow flakes. *J. Atmos. Sci.*, **47**, 584–591, doi:10.1175/1520-0469(1990)047<0584:AWTATS>2.0.CO;2.
- Nakanishi, M., and H. Niino, 2004: An improved Mellor–Yamada level-3 model with condensation physics: Its design and verification. *Bound.-Layer Meteor.*, **112**, 1–31, doi:10.1023/B:BOUN.0000020164.04146.98.
- Olson, W. S., P. Bauer, N. F. Viltard, D. E. Johnson, W.-K. Tao, R. Meneghini, and L. Liao, 2001: A melting-layer model for passive/active microwave remote sensing applications. Part I: Model formulation and comparison with observations. *J. Appl. Meteor.*, **40**, 1145–1163, doi:10.1175/1520-0450(2001)040<1145:AMLMFP>2.0.CO;2.
- Peters, G., B. Fischer, and T. Andersson, 2002: Rain observations with a vertically looking Micro Rain Radar (MRR). *Boreal Environ. Res.*, **7**, 353–362. [Available online at <http://www.biral.com/imagprod/downloads/ref4ber7-353.pdf>.]
- Phillips, V., A. Khain, and A. Pokrovsky, 2007: The influence of time-dependent melting on the dynamics and precipitation production in maritime and continental storm clouds. *J. Atmos. Sci.*, **64**, 338–359, doi:10.1175/JAS3832.1.
- Pruppacher, H. R., and J. D. Klett, 1997: *Microphysics of Clouds and Precipitation*. 2nd ed. Oxford University Press, 914 pp.
- Rasmussen, R. M., and A. J. Heymsfield, 1987: Melting and shedding of graupel and hail. Part I: Model physics. *J. Atmos. Sci.*, **44**, 2754–2763, doi:10.1175/1520-0469(1987)044<2754:MASOGA>2.0.CO;2.
- , V. Levizzani, and H. R. Pruppacher, 1984: A wind tunnel and theoretical study of the melting behavior of atmospheric ice particles: III. Experiment and theory for spherical ice particles of radius > 500 μm . *J. Atmos. Sci.*, **41**, 381, doi:10.1175/1520-0469(1984)041<0381:AWTATS>2.0.CO;2.
- Schols, J. A., J. A. Weinman, R. E. Stewart, and R. P. Lawson, 1995: The retrieval of dry and wet snow distributions from SSM/I measurements and MM5 forecast results. *Proc. 1995 Int. Geoscience and Remote Sensing Symp.*, Florence, Italy, IEEE, 887–889. [Available online at <http://ieeexplore.ieee.org/xpl/articleDetails.jsp?arnumber=521087>.]
- Smith, C. J., 1986: The reduction of errors caused by bright bands in quantitative rainfall measurements made using radar. *J. Atmos. Oceanic Technol.*, **3**, 129–141, doi:10.1175/1520-0426(1986)003<0129:TROECB>2.0.CO;2.
- Szyrmer, W., and I. Zawadzki, 1999: Modeling of the melting layer. Part I: Dynamics and microphysics. *J. Atmos. Sci.*, **56**, 3573–3592, doi:10.1175/1520-0469(1999)056<3573:MOTMLP>2.0.CO;2.
- Tao, W.-K., J. R. Scala, B. Ferrier, and J. Simpson, 1995: The effect of melting processes on the development of a tropical and a midlatitude squall line. *J. Atmos. Sci.*, **52**, 1934–1948, doi:10.1175/1520-0469(1995)052<1934:TEOMPO>2.0.CO;2.
- Tokay, A., A. Kruger, and W. F. Krajewski, 2001: Comparison of droplet size distribution measurements by impact and optical disdrometers. *J. Appl. Meteor.*, **40**, 2083–2097, doi:10.1175/1520-0450(2001)040<2083:CODSDM>2.0.CO;2.
- , P. G. Bashor, and K. R. Wolff, 2005: Error characteristics of rainfall measurements by collocated Joss–Waldvogel disdrometers. *J. Atmos. Oceanic Technol.*, **22**, 513–527, doi:10.1175/JTECH1734.1.
- Yuter, S. E., and R. A. Houze Jr., 1995: Three-dimensional kinematic and microphysical evolution of Florida cumulonimbus. Part I: Spatial distribution of updrafts, downdrafts, and precipitation. *Mon. Wea. Rev.*, **123**, 1921–1940, doi:10.1175/1520-0493(1995)123<1921:TDKAME>2.0.CO;2.
- Zawadzki, I., W. Szyrmer, C. Bell, and F. Fabry, 2005: Modeling of the melting layer. Part III: The density effect. *J. Atmos. Sci.*, **62**, 3705–3723, doi:10.1175/JAS3563.1.